

Structure of the Amide I Band of Peptides Measured by Femtosecond Nonlinear-Infrared Spectroscopy

Peter Hamm, Manho Lim, and Robin M. Hochstrasser*

Department of Chemistry, University of Pennsylvania, Philadelphia, Pennsylvania 19104

Received: February 27, 1998; In Final Form: April 29, 1998

Femtosecond infrared (IR) pump probe and dynamic hole burning experiments were used to examine the ultrafast response of the modes in the 1600–1700 cm^{-1} region (the so-called amide I modes) of *N*-methylacetamide (NMA) and three small globular peptides, apamin, scyllatoxin, and bovine pancreatic trypsin inhibitor (BPTI). A value of 16 cm^{-1} was found for the anharmonicity of the amide I vibration. Vibrational relaxation of the amide I modes of all investigated peptides occurs in ca. 1.2 ps. An even faster value of 450 fs is obtained for NMA, a model for the peptide unit. The vibrational relaxation is dominated by intramolecular energy redistribution (IVR) and reflects an intrinsic property of the peptide group in any environment. Dynamic hole burning experiments with a narrow band pump pulse which selectively excites only a subset of the amide I eigenstates reveal that energy migration between different amide I states is slow compared with vibrational relaxation. Two-dimensional pump–probe (2D-IR) spectra that display the spectral response of the amide I band as a function of the frequency of the narrow band pump pulse show that the amide I states are nevertheless delocalized along the peptide backbone. A simple excitonic coupling model describes the nonlinear pump–probe spectrum, and it reproduces the experimental 2D-IR spectra. It is estimated that the accessible peptide excitons are delocalized over a length of ca. 8 Å.

1. Introduction

Proteins have vibrational spectra that contain important details of their structure. In particular, the protein secondary structures must be the main factors determining the force fields and hence the spectra of the amide bands, which arise from motions of the peptide atoms. It is for this reason that the vibrational spectra of the amide I band in the 6 μm region, which involve mainly the C=O stretching displacements of the peptide backbone with contributions from the CN and NH motions¹, have been widely used as marker modes of secondary structure. For example, proteins containing mostly β -sheets have amide I bands at lower frequency than those containing mostly α -helices. In particular the amide I transitions are ideal for infrared (IR) spectroscopy since the motions have extremely large dipole derivatives, and they are clearly distinguishable from vibrational transitions of the amino acid side chains. In fact the amide I vibrational subspace is usually thought of as decoupled from the remaining vibrational modes of a protein.

A number of different approaches have been used to address the relationships between the structures and the vibrational spectra of peptides. Normal mode descriptions were developed to calculate all the vibrational eigenmodes of a protein^{1–4} based on empirical force fields deduced from spectroscopic data¹ or from ab initio calculations on small model systems such as hydrogen bonded *N*-methylacetamide (NMA)⁵ and dipeptides.^{6,7} From studies of the vibrations of highly symmetric polypeptides, Krimm et al. showed the importance of transition dipole–dipole coupling in the spectra of the amide I band¹. In one recent approach^{8,9} the amide I vibrational subspace was treated as a molecular exciton band¹⁰ with the individual monomeric peptide groups coupled only by the transition dipole–dipole interactions. The connection between the secondary structure of the peptide backbone and the absorption spectrum of the amide I band is

determined by the angular and distance dependence of the dipole interactions. Qualitative agreement was found between this very simple model and measured FTIR spectra for some midsize proteins.⁸ Finally, there are empirical methods that use the experimental vibrational spectra of proteins with known structure, to predict the presence of various secondary structures in other proteins (see for example ref 11 and references cited therein).

Although the IR spectrum of the amide I band of proteins with different structures do differ, these spectra do not reveal separate peaks for the different amide modes which together constitute the amide I band. Homogeneous and inhomogeneous broadening mechanisms smear out the spectrum, resulting in a relatively broad band with only a weak substructure in the form of unpronounced shoulders. Resolution enhancing techniques such as taking the second derivative or deconvolution of the spectra cannot overcome this problem. Thus, there is limited experimental information available with which to test the various models. In the present work nonlinear-IR spectroscopy is developed that can uncover additional information regarding the composition of the amide I vibrations of peptides. We demonstrate that nonlinear spectroscopy is more sensitive to the three-dimensional structure of the peptide than is linear-IR absorption spectroscopy.

The amide I states of symmetric model peptides are known to be delocalized with the dominant coupling being the transition dipole interaction.¹ However, the extent of delocalization of the amide I wave functions of natural peptides is less clear. The intrinsic disorder of natural peptides will tend to localize the vibrational excitations, but there is as yet insufficient experimental data with which one could establish a quantitative picture. In general, the linear absorption spectra of proteins do not manifest splittings resulting from the transition dipole interaction, such as those that occur in highly symmetric

aggregates. It is shown here that infrared pump probe spectroscopy is capable of yielding much more detailed information regarding this and other questions related to delocalization.

Vibrational energy migration and energy relaxation within a protein are of crucial importance to the energetics of biological reactions. Energy dissipation by protein nuclear motions must strongly influence the rates, pathways, and efficiencies of chemical reactions involving proteins. Some of the many types of processes that must involve coupling to protein modes include the following: barrier crossings, which may be important in enzyme reactions; electron transfer, which are ubiquitous in biology; and conformational dynamics. The possible roles of peptide motions in storing and transporting vibrational energy in such examples are not known. For example, it is not known whether vibrational energy transport through a peptide occurs entirely by thermal diffusion following very fast intramolecular vibrational relaxation or whether directed coherent transport needs to be considered. The only vibrational energy relaxation rate measured for a particular vibrational state in a protein is for the bound carbon monoxide in heme proteins, which relaxes in ca. 20 ps.^{12,13} No information is yet available for relaxation of peptide modes, which is another motivation for the present study.

Three peptides were selected for this work: apamin, a small neurotoxic peptide component of the honey bee venom; scyllatoxin, a scorpion toxin with high affinity for apamin sensitive potassium channels; and BPTI, bovine pancreatic trypsin inhibitor. These peptides were chosen for their variety of structural motifs and because they are small enough that theoretical modeling is feasible. They each have a well-characterized globular structure in solution, and their secondary structure motifs are known. Their structures are shown as inserts in Figure 1. Apamin, one of the smallest globular peptides known,¹⁴ has 18 amino acids, a short α -helix and a β -turn. Scyllatoxin, with 31 amino acids, is the smallest known natural peptide containing both an α -helix and a β -sheet.^{15,16} BPTI is about twice as large as scyllatoxin, has 58 amino acids, and also contains both α -helix and β -sheet peptide motifs. Its structure is well-characterized;^{17,18} molecular dynamics simulations exist¹⁹ as well as normal mode calculations.^{20–22}

2. Materials and Methods

Infrared Laser System. The IR setup is described in somewhat more detail in ref 23. Briefly, a white light seeded, two stage BBO-OPA was used to split the output pulses of a Ti:S amplifier (800 nm, 500 μ J, ca. 80 fs) into a signal and an idler pulse which subsequently were difference frequency mixed in a AgGaS₂ crystal to generate short and intense IR pulses around 1650 cm^{-1} (bandwidth, 130 cm^{-1} ; pulse duration, 180 fs; energy, ca. 1 μ J). The IR pulses were essentially chirp free.²⁴ Pump and probe pulses were separated by a wedged CaF₂ window. The pump pulses were sent to a variable delay line. Both beams were focused onto the sample with a 10 cm off-axis parabolic mirror, yielding a spot size of ca. 100 μ m for the probe and 150 μ m for the pump. To cover the whole spectral range of interest (1580–1700 cm^{-1}), a 32 channel MCT detector array was used to construct an infrared multichannel detector. The array was mounted on the focal plane of a 270 mm spectrograph with a 120 L/mm grating, resulting in a spectral resolution of 3.8 cm^{-1} /pixel. Due to the excellent short-term stability of the IR light source (≤ 0.5 –1% root mean square), no referencing with an independent detector was necessary. Chopping the excitation light beam at half the repetition rate of the laser system eliminated long-term drifts of the IR

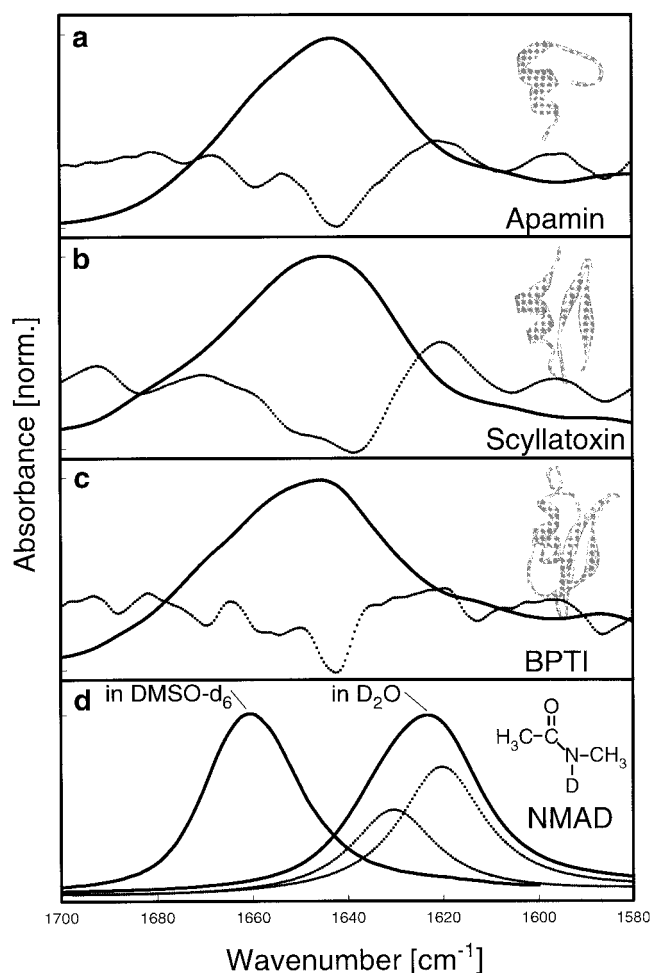


Figure 1. Linear absorption spectra (solid lines) and their second derivatives (dotted lines) of apamin, scyllatoxin, bovine pancreatic trypsin inhibitor (BPTI), and deuterated *N*-methylacetamide (NMAD) in the spectral range of the amide I band. The background absorption of the solvent is subtracted from these spectra. The inserts show ribbon structure of the peptides. NMAD was measured both in D₂O and DMSO-*d*₆ as solvent.

intensity. An overall sensitivity of the order 10^{-5} optical density units (OD, root mean square) was achieved. The anisotropy measurements were carried out by rotating the polarization of the probe beam with two sequential wire grid polarizers.

Two types of transient experiments have been performed: In a broad band pump experiment the whole amide I band was excited. In this case, a significant solvent (D₂O) signal around delay zero caused by cross-phase modulation due to the Kerr effect disturbs the measurement, similar to what is found in vis-pump-IR-probe experiments.²⁵ In addition, a small solvent background due to direct excitation of D₂O was observed (<0.1 mOD) also at later times which develops on a subpicosecond time scale. The D₂O signal was measured independently and subtracted from the data in order to reveal the pure peptide signal. The Kerr signal was used for the determination of delay zero and cross-correlation width (typically 200–250 fs).

In a second type of experiment, spectrally narrow holes were burned into the amide I band. Tunable spectrally narrow pump pulses were generated by filtering the original pulses with a tunable IR-Fabry-Perot filter which was constructed from two partial reflectors ($R = 90\%$), one of which was mounted on a stepping motor controlled translation stage (Melles Griot, nanomover). A peak transmission of ca. 30% was achieved. The pump wavelength could be tuned by fine adjustment of

the distance between both mirrors in steps of 100 nm. In addition, by choosing the order of interference, the spectral width could be adjusted. A minimal spectral width of $9\text{--}10\text{ cm}^{-1}$ for a free spectral range of 120 cm^{-1} (i.e. the full spectral range covered by the detector) was achieved. The resulting pump pulses had an asymmetric pulse shape with a fast rising edge limited by the pulse duration of the original pulse and a falling slope which decayed exponentially with a decay constant given by the reflectivity and the separation of the mirrors (ca. 1 ps in the present experiments). No significant solvent signal disturbed these measurements because the pump intensity was ca. 100 times smaller than in the broad band experiment.

Only ca. 300 nJ of energy was used in the pump beam for the broad band experiment, yielding an excitation density of ca. 30%. Higher excitation density resulted in a nonlinear response due to double excitation within one peptide. The total pump energy used for the hole burning experiment was 25 nJ, but the spectral intensity was roughly the same as in the broad band experiment. The absolute size of the anisotropy might be influenced by the relatively high excitation density, but the kinetics of the anisotropy should be minimally affected.

Samples. Three peptides have been investigated: BPTI, apamin, and scyllatoxin. The samples were purchased from Sigma. All experiments were done in D_2O in order to reduce the solvent background absorption. H–D exchange of the peptide groups was performed by dissolving the samples in D_2O , keeping them for at least $\frac{1}{2}$ h at room temperature, lyophilizing them again, and repeating this procedure twice. Heating the sample for a more complete H–D exchange was tested but did not result in a difference in the absorption spectrum. The absorption spectra of scyllatoxin and BPTI showed a sharp absorption peak around 1680 cm^{-1} . This peak originated from the salt of trifluoroacetic acid which commonly is used as a buffer during preparation. In these cases, the pH of the samples was lowered to pH = 2 by adding small amounts of HCl and the sample was lyophilized which also causes trifluoroacetic acid to evaporate. This procedure was repeated twice. Afterward, the pH was adjusted to pH = 5 by adding small amounts of NaOH. Apamin was measured at pH 7. NMA was purchased from Aldrich and used without further purification. NMA automatically is deuterated in D_2O (=NMAD). To deuterate NMA for the measurement in dimethyl- d_6 sulfoxide ($\text{DMSO-}d_6$), NMA was first dissolved in D_2O and lyophilized, this procedure being repeated twice, and then dissolved in $\text{DMSO-}d_6$.

The samples were held in a CaF_2 cuvette (spacing, $25\text{ }\mu\text{m}$) which was rotated during the experiment in order to prevent local heating. All experiments were performed at room temperature. For the peptides, a concentration of ca. $30\text{ }\mu\text{g}/\mu\text{L}$ was used, corresponding to a concentration of amino acids of ca. 270 mM or, depending on the size of the peptide, a concentration of peptides between 5 mM (BPTI) and 15 mM (apamin), respectively. NMAD was measured at a concentration of ca. 150 mM.

3. Results

3.1. Absorption Spectra. Linear absorption spectra of the amide I band of the three peptides are shown in Figure 1a–c together with their second derivatives (the D_2O background absorption is subtracted). Although the spectra do differ slightly in detail, best seen in the second derivative signal, overall these spectra are very similar. They have a peak at ca. 1645 cm^{-1} and a bandwidth of $30\text{--}40\text{ cm}^{-1}$ and have some unresolved substructure showing up only as weak shoulders. The substructure is more prominent in the second derivative spectrum.

Figure 1d shows the absorption spectrum of NMAD in D_2O and $\text{DMSO-}d_6$. In D_2O , the total bandwidth of the absorption line is 28 cm^{-1} (full width at half-maximum, fwhm). The band does not have a simple Lorentzian or Gaussian line shape but exhibits a shoulder on the high-frequency side. A multiline fit yields two Lorentzian contributions which are separated by 10 cm^{-1} and which each have a bandwidth of 21 cm^{-1} . These contributions are shown in Figure 1d as dotted lines. In $\text{DMSO-}d_6$, the peak position shifts by ca. 40 cm^{-1} to higher frequencies, the total bandwidth is somewhat smaller (23 cm^{-1}), and the shape is more symmetric.

3.2. Background: Femtosecond IR Pump–Probe Response. To facilitate the discussion of the experimental results of pump–probe measurements on the amide band, a brief description of the basic phenomena that can be expected from such experiments on multilevel systems is needed. The pumped and probed system will be assumed to consist of a set of n levels near the $\nu = 0 \rightarrow n = 1$ amide transition and a set of $n(n + 1)/2$ levels at approximately twice that frequency. The set at the fundamental frequency corresponds to one quantum for each of the n amide groups, while those in the two-quantum region include excitations of two amide groups and the overtone states of each group. A detailed description of a model for the energies of these states will be given later. The pumping process in our case incorporates a pulse that is short compared to the inverse width of the amide I band, and therefore all the possible transitions involving the one-quantum step can be excited. However in such problems the signals depend also on the properties of the probe pulse. This is because the fields generated by the third-order nonlinear interaction, which are measured by the detector, can arise from different time orderings of the incident fields chosen from either the pump or the probe. Since the pump–probe and dynamic hole burning experiments use pulses with different spectra, different processes can be involved. The traditional way of categorizing the various molecule field interactions is to employ double-sided Feynman diagrams to illustrate the time evolution of the density matrix that is measured in such experiments.^{26–28}

Figure 2 shows the sixteen *basic types* of diagrams (see figure caption for further explanation) that need to be considered. There are four such representative diagrams for each of the processes in the pump–probe experiment: namely, the appearance of new absorptions a1 to a4, direct two-photon absorptions da1 to da4, stimulated emissions se1 to se4, and loss of ground state absorption, known as bleachings b1 to b4. They are all chosen for the case where the generated field propagates in the direction of the input probe field. Two of each of the four diagrams representing a, se, and b correspond to the system interacting with fields in the order pump/pump/probe, one to the ordering pump/probe/pump, and one to probe/pump/pump. The diagrams for da only involve the time orderings pump/probe/pump and probe/pump/pump. Using excited-state absorption as an example, diagrams a1 and a2 correspond to the creation of populations and coherences in the one-quantum states which then undergo absorption to the two-quantum region. Diagram a3 corresponds to the probe coupling to the system between the two pump field interactions. Diagram a4 arises when the probe field is the first to interact. In all these cases a dephasing occurs after the interaction with the first two fields due to the interference of the $n(n - 1)$ oscillatory density matrix elements that are created. This dephasing occurs on the time scale of the inverse of the width of the distribution of frequencies spanned by the intermediate states, assuming a more or less random distribution of levels. We consider this time to be

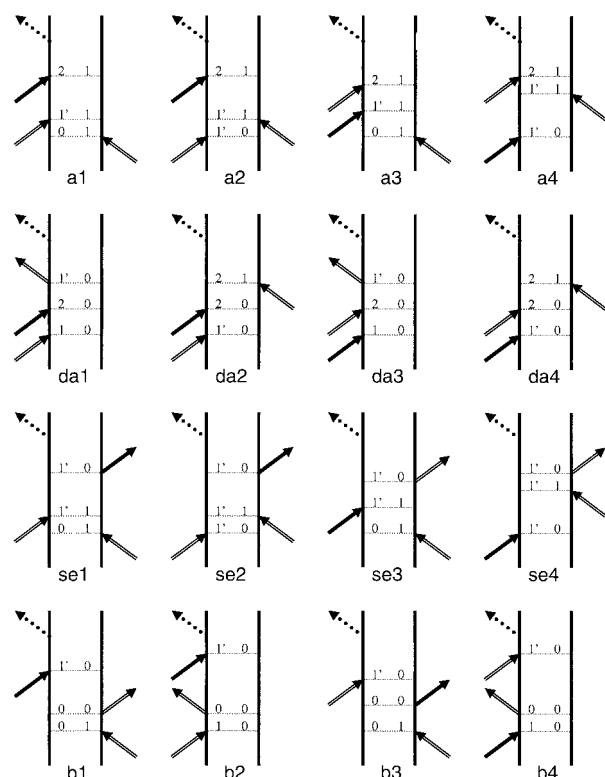


Figure 2. Sixteen *basic types* of double-sided Feynman diagrams possible for a femtosecond pump-probe experiment on a multilevel system where a set of $\nu = 0 \rightarrow \nu = 1$ transitions and a set of $\nu = 1 \rightarrow \nu = 2$ transitions are both resonant with the spectrally broad pump and probe pulse. The one-quantum region consists of n substates (denoted 1 or 1') and the two quantum region of $n(n+1)/2$ substates are denoted as 2. The left and right vertical lines represent the ket and bra of the density matrix, respectively. The double-lined arrows represent an interaction with the field of the pump pulse, the solid arrows an interaction with the probe field and the dotted line the generated third-order polarization. All diagrams shown correspond to the generated field propagating in the direction of the input probe field.

relatively short compared with population relaxation between the levels. In that case after dephasing, diagrams a1 and a2 describe a conventional transient absorption involving only the diagonal elements. The decay of the signal corresponds to the population relaxation times of the one-quantum region states. Diagram a3 represents a transient absorption signal that exists only during the pump pulse width. Since the pump is shorter than the dephasing time, this contribution is a coherent two-photon absorption. Diagram a4 is an absorption contribution to the well-known perturbed free induction decay signal that occurs before time zero^{29–32} in pump-probe signals when the dephasing of the two levels being coupled by the light field is longer than the pulse widths. The analysis is quite similar for the other processes. The direct two-photon absorption terms da1 and da2 only contribute to the absorption during the period that the pump and probe pulses overlap, while da3 and da4 only contribute before time zero. These are two-photon processes that do not involve the creation of populations or coherences in the intermediate one-quantum region. Two of the stimulated emission diagrams, se1 and se2, give the conventional signal which comes only from populations after dephasing of the intermediate states, the diagram se3 contributes only during the period the pump pulse is present, and se4 contributes only before time zero to give a stimulated emission contribution to the perturbed free induction decay. The signal contributions due to bleaching of the ground-state signal break down in an analogous manner and are displayed as b1 to b4 in Figure 2.

Since the pump pulses are longer in the dynamic hole burning experiment, the processes which contribute to the perturbed free induction decay (a4, da3, da4, se4, b4) and those which contribute to the coherent two-photon absorption (a3, da1, da2, se3, b3) are less important in this type of experiment. This is because these processes depend on coherence between the ground state and the one-quantum states and thus they disappear when the pulses become long compared with the inverse inhomogeneous bandwidth of the one-quantum band.

3.3. Broad Band Pump Experiment. The results of the broad band-pump experiment are shown in Figure 3 as 3D plots. All of the processes described in Section 3.2 are evident in the data. The pump pulse was centered at the absorption maximum of the amide I band of the sample. Since the bandwidth of the pump pulses is much broader than that of the amide I band, all frequency components of the absorbing system are excited essentially with the same pump light intensity. The pump-probe signals of all peptides have many features in common. At negative delay times (probe pulse before pump pulse), the signal grows in on a time scale which is not pulse width limited but given by the inverse bandwidth of the absorption band. In addition, an oscillatory behavior is seen in all cases. The oscillation frequencies are determined by the detuning between the probe frequency selected by the monochromator and the peak of the absorption band. These signals correspond to the perturbed free induction decay effect discussed above^{29–32} and diagrammed in a4, da3, da4, se4, and b4. The negative and positive difference spectral regions all show a part that decays on the time scale of the pulse width. These signal contributions must arise from the processes diagrammed in a3, da1, da2, se3, and b3.³³ When the probe pulse arrives after the pump pulse with delay times in excess of 250 fs, only the diagrams a1, a2, se1, se2, b1, and b2 remain and the signal is attributed to population of the one-quantum states. At this stage, the signal is free from effects which are due to coherence between the ground state and the one-quantum states but not necessarily free from coherence between the one-quantum states. In this paper we will focus only on processes that occur *after* 250 fs and leave the discussion of the coherent effects for a future paper which will include other types of coherent infrared nonlinear responses that probe the coherences more effectively than pump-probe experiments.

A negative signal (bleach) around 1655 cm^{-1} and a positive signal (excited-state absorption) peaked around 1630 cm^{-1} are observed in all peptides. They decay on a 1 ps time scale which must correspond to the process of vibrational relaxation. Cuts along the frequency and the time axis provide a more detailed picture of the processes involved.

3.3.1. Kinetics of the Magic Angle and Anisotropy Decays. Figure 4 shows the temporal decays of the positive and rises of the negative absorption changes (evaluated for magic angle). Figure 5 shows the anisotropy of these signals for the peptides. The data are an average over a 15 cm^{-1} broad frequency range, each of which is centered at a frequency where the positive or negative signal is peaked. Both pump-probe magic angle and anisotropy data were fit to a biexponential function:

$$A = a_1 \exp(-t/\tau_1) + a_2 \exp(-t/\tau_2) \quad (1)$$

The resulting fit parameters are summarized in Table 1. In most cases both terms were needed to obtain a satisfactory fit, but the positive absorption signal in scyllatoxin and the anisotropy of the weaker BPTI signal are reasonable fit by a single-exponential function. The fitting parameters vary slightly between the different peptides. As a general trend, the faster

TABLE 1: Fit Parameter for the Data Shown in Figures 4 and 5

	apamin				scyllatoxin				BPTI				NMAD in D ₂ O			
	neg	aniso	pos	aniso	neg	aniso	pos	aniso	neg	aniso	pos	aniso	neg	aniso	pos	aniso
τ_1/ps	0.4	0.5	0.4	0.2	0.4	0.3		0.3	0.3		0.7	0.6	0.45	6	0.43	8
τ_2/ps	1.2	∞	1.1	2.8	1.2	2.1	1.0	15	1.1	2.2	1.5		4		3	
α_1/α_2	1.1	3.0	0.6	2.6	0.7	2.3		3.0	0.65		0.55		5		4	

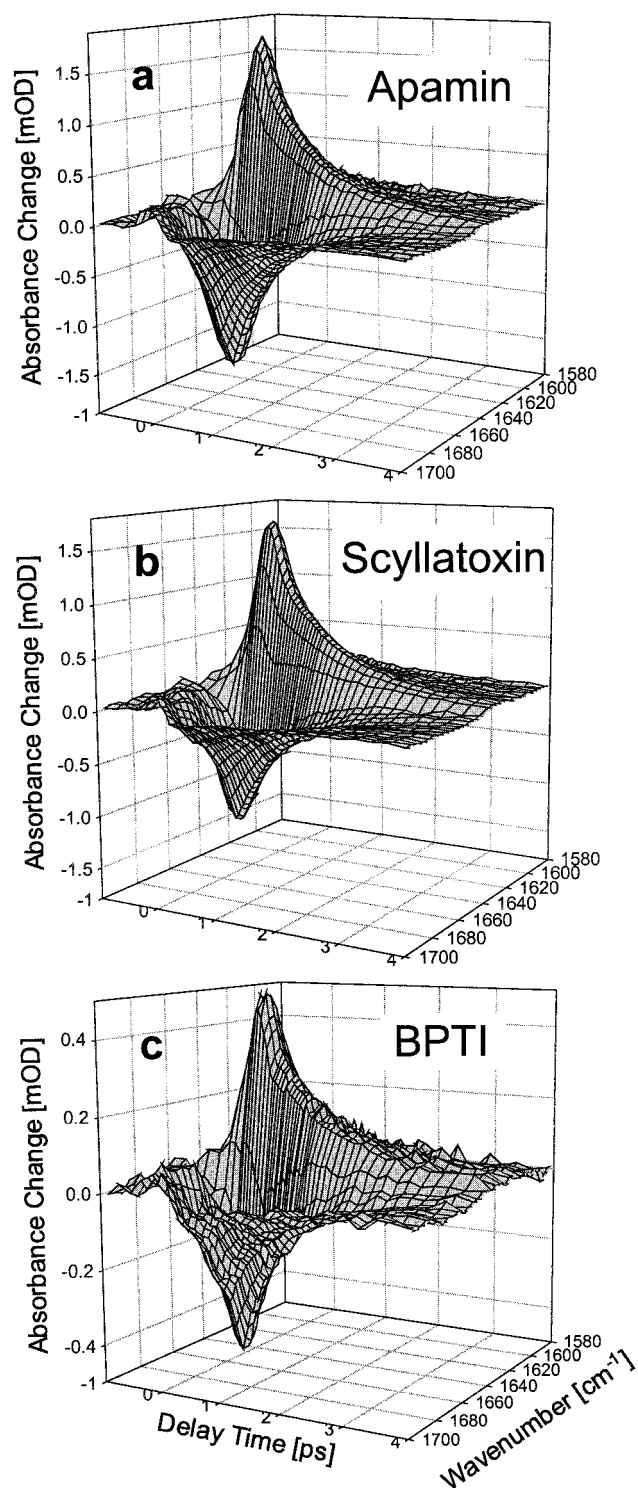


Figure 3. 3D plot of the frequency dependent absorption change of apamin (a), scyllatoxin (b), and BPTI (c) after exciting the sample with a broad band IR pump pulse. The signal was determined for magic angle orientation of pump and probe beams.

time constant τ_1 of the magic angle signals is in the range of 300–500 fs while the slower time constant τ_2 is approximately 1.2 ps. The amplitude of the faster time constant is in general

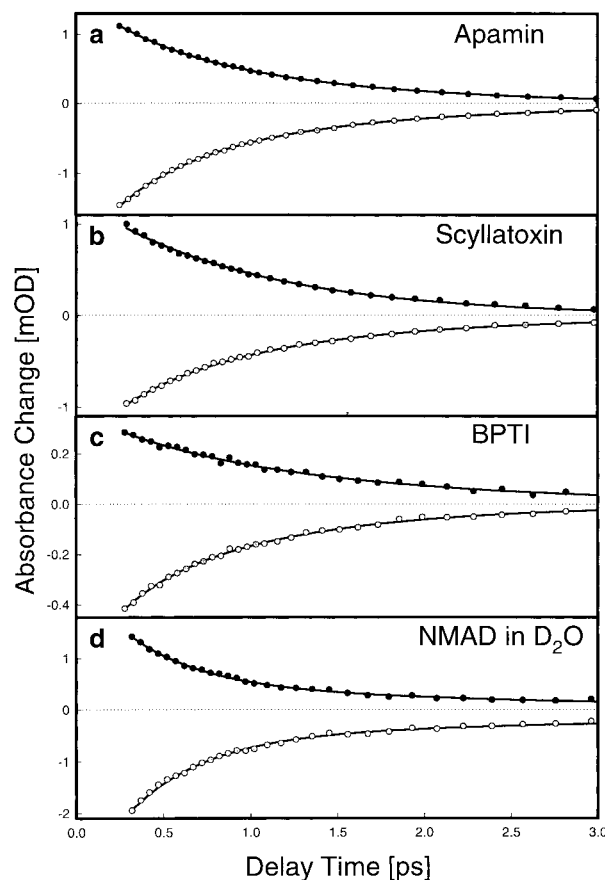


Figure 4. Time traces of the magic angle absorption change and the anisotropy of these absorption signals. The signals are an average over a frequency range of 15 cm^{-1} , each of which is centered around the peak of the bleaching part (gray circles) and the excited-state absorption (black circles). The curves are fit to biexponential model functions. The fit parameters are summarized in Table 1.

somewhat smaller than that of the slower component (a_1/a_2 around 0.6). The faster time constant found in the anisotropy signals is similar to that of the magic angle signals. The second anisotropy component is slower than that found in the magic angle signal and is distributed over a wide range from 2.1 ps to essentially a constant. Also, the amplitude of the faster anisotropy component is 2–3 times larger than that of the slower one.

Figure 4d shows the magic angle pump probe signal of the amide I mode of NMAD in D₂O. At first sight, the decay of the signal looks similar to that seen for the peptides. However, the biexponential character is more pronounced in NMAD, which has a dominating fast component (450 fs) and a slower component (4 ps) whose amplitude is only ca. 20% of the total signal. The anisotropy signal shown in Figure 5d is completely different from that found in the peptide samples in that it decays on a slow time scale of 6 ps. The fit parameters are listed in Table 1.

3.3.2. Transient Difference Spectra. The solid lines in Figure 6 a–c represent the transient difference spectra of apamin, scyllatoxin, and BPTI measured 400 fs after excitation. Quali-

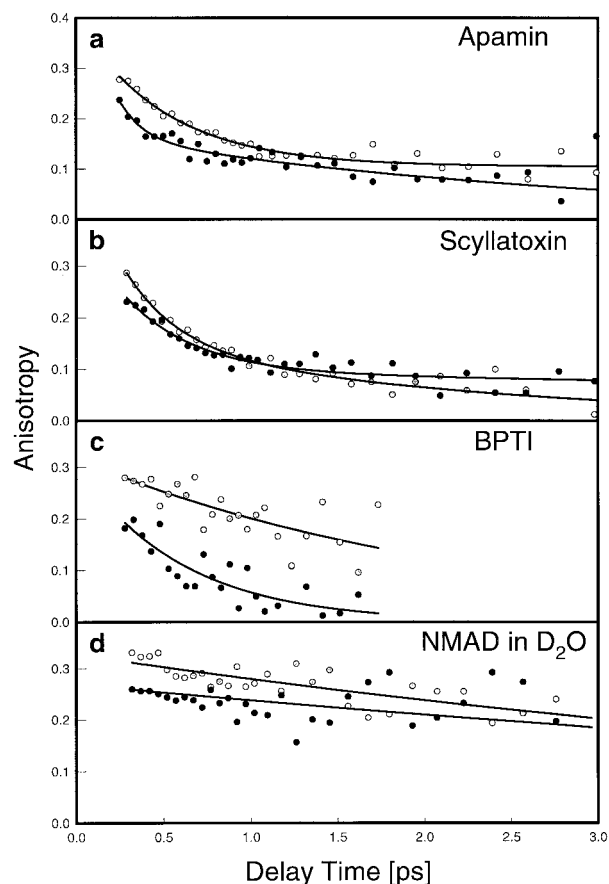


Figure 5. Anisotropy of the data shown in Figure 4. The signals are an average over a frequency range of 15 cm^{-1} , centered around the peak of the bleaching portion (gray circles) and the excited-state absorption (black circles). The fit parameters are summarized in Table 1.

tatively, these spectra are very similar. There is negative signal (bleach) between 1700 and ca. 1640 cm^{-1} and a new absorption at lower frequencies. Both bands exhibit a weak unresolved substructure.

When exciting a vibrator from its ground state ($\nu = 0$) to the first excited state ($\nu = 1$), a transient absorption signal is expected which is anharmonically shifted to a lower frequency. Figure 6d shows transient difference spectra of NMAD in $\text{DMSO-}d_6$. The anharmonicity of the amide I mode of NMAD was deduced from the transient difference spectrum by fitting the difference spectrum with the negative equilibrium spectrum and a frequency shifted positive Lorentzian band. The peak position and the width of the negative band was obtained from the equilibrium absorption spectrum (Figure 1d) and was held fixed during fitting. This procedure yielded an anharmonic frequency shift of 16 cm^{-1} . A result obtained from NMAD in D_2O was considered less reliable because the spectrum of NMAD in D_2O is much broader than the anharmonic frequency shift, and it has a doublet structure.

The amide I bands of the peptides are superpositions of many vibrational levels having similar frequencies, so a loss of absorption (bleach) is expected at the high-frequency side and an absorption increase at the low-frequency side of the absorption spectrum, but the separation is not expected to be the anharmonicity. If the amide I band were composed of a sufficiently large number of vibrational modes, the transient difference spectrum should be similar to the first derivative of the linear absorption spectrum when the anharmonic shift is small and the same for all modes, and all modes are excited

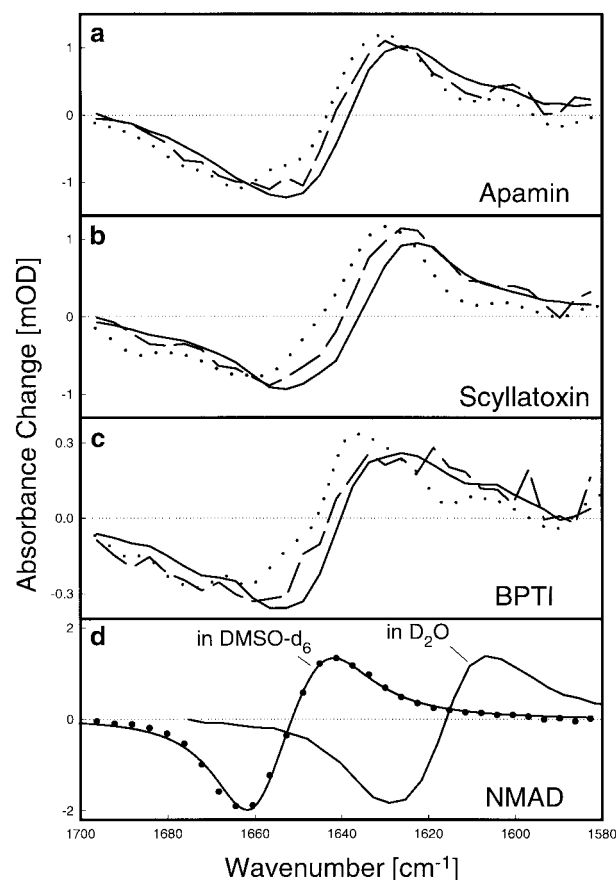


Figure 6. (a–c) Transient difference spectra of apamin, scyllatoxin, and BPTI measured 400 fs after vibrational excitation (solid lines) and 2.4 ps after excitation (dashed lines). The 2.4 ps data are properly scaled. The time-resolved data are compared to the first derivative of the FTIR absorption spectrum (dotted line). (d) NMAD was measured both in D_2O and $\text{DMSO-}d_6$ as solvents. The difference spectrum measured for NMAD in $\text{DMSO-}d_6$ (circles) was fit by a negative equilibrium spectrum and a frequency shifted positive Lorentzian band (solid line). The peak position and the width of the negative band were obtained from the equilibrium absorption spectrum and held fixed during fitting.

equally. In Figure 6a–c, the time-resolved spectra are compared with the derivative of the absorption spectrum (dotted line, properly scaled). The 400 fs spectrum and the derivative spectrum clearly are *not* the same. Both the isosbestic point and the shape are different. These deviations indicate that the foregoing assumptions are oversimplified and do not properly describe the anharmonicity of the amide I mode.

Also shown in Figure 6a–c are the difference spectra measured 2.4 ps after excitation (dashed lines). These spectra are linearly scaled by a factor of $\times 7$ in order to facilitate their comparison with the 400 fs spectra. Interestingly, besides the amplitude changes shown in Figure 4 there are also changes in the position of the isosbestic point and in the shape of the difference spectra. In each case, a frequency upshift (ca. 5 cm^{-1}) is found at 2.4 ps delay. This spectral shift can also be revealed from the kinetic traces which yield decay constants which are slightly frequency dependent. The effect, however, is more evident by comparing the spectra as in Figure 6.

3.4. Dynamic Hole Burning. In a second type of experiment, the samples were pumped by a narrow band pump pulse (bandwidth, 10 cm^{-1}) in order to selectively excite only a subset of the vibrational modes within amide I band. Parts a–c of Figure 7 show transient difference spectra after pumping at four different frequency positions: (a) at the very high-frequency side of the amide I band, (b) at the center of the band, and (c)

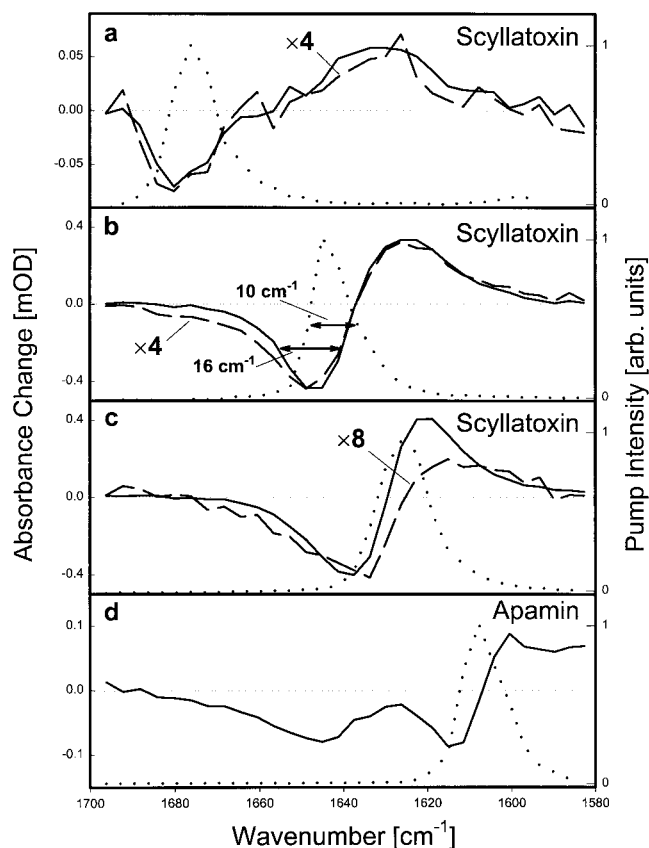


Figure 7. Result of the dynamic hole burning experiment where the samples were pumped with a narrow band pump pulse (spectrum of the pump pulse shown as a dotted line). The responses at “delay zero”³⁴ (solid line) and 2.4 ps after excitation (dashed lines) are shown. The 2.4 ps spectra are scaled. The scaling factor necessary to match the amplitude of both spectra is dependent on the pump frequency. It is $\times 4$ when pumping the high-frequency side and center frequency of the band (a and b) and $\times 8$ when pumping the low-frequency side (c).

and d) at two positions at the low-frequency side of the band. The spectra of the pump pulses for each case are shown as dotted lines. The transient spectra measured at “delay zero”³⁴ are shown as a solid line and those measured 2.4 ps after excitation as dashed lines. The 2.4 ps data are linearly scaled in order to facilitate their comparison with the zero delay spectra.

A number of extremely interesting features can be identified from these spectra. The data for scyllatoxin and apamin show that it is indeed possible to burn holes into the amide I band, proving that the amide I band is composed of a superposition of transitions which are narrower than the full bandwidth. The position of the hole depends on the position of the pump pulse. In other words, the amide I band has underlying transitions that are narrower than the total bandwidth of the amide I band. Energy redistribution among the different vibrational levels composing the amide I band must be slow compared with the time scale of this measurement. The width of the spectral hole (16 cm^{-1} for scyllatoxin, see Figure 7 b) is broader than the 10 cm^{-1} width of the inducing pump pulse. This finding indicates that dephasing of the underlying amide I vibrational is more rapid than the pulse duration.

The transient absorption spectrum strongly depends on the center frequency of the pump pulse. The frequency separation between bleach and excited-state absorption is largest when the pump is at the highest frequency (Figure 7a). For lower frequency excitation the bleach and the excited-state absorption overlap to such an extent that the resulting negative signal appears at a higher frequency position than the peak of the pump

pulse spectrum (Figure 7c). Also the width of the excited-state absorption spectrum depends on the frequency of the pump pulse, being broadest for the highest frequency pump ($30\text{--}40\text{ cm}^{-1}$) and becoming narrower as the pump frequency is reduced.

The width of the spectral hole increases with delay time between pump and probe pulses. However, the amount of the broadening depends on the frequency position of the pump pulse. It is negligible for the high-frequency pump (within the signal-to-noise level) and becomes most prominent in the low-frequency pump experiment. In addition, the decay rate of the spectral hole depends on the pump frequency. This effect is monitored by the scaling factor needed to match the delay zero and the 2.4 ps difference spectra in Figure 7a–c: The scaling factor is $\times 4$ in Figure 7a,b (high and center frequency pump) and $\times 8$ in Figure 7c (low-frequency pump).

A double peak structure occurs in the probe spectra when the very low-frequency edge of the amide I band (around 1610 cm^{-1}) is pumped. Figure 7d shows this effect for apamin where it is more prominent than for scyllatoxin.

In Figure 8, two-dimensional infrared (2D-IR) pump–probe spectra of apamin and scyllatoxin are shown as contour plots. These 2D-IR spectra are assembled by measuring the transient difference spectra as a function of the peak frequency of the pump pulse. Slightly broader (12 cm^{-1}) and accordingly shorter pump pulses than those used in the experiments described above were used to obtain these spectra. The data in Figure 8 refer to the early delay time situation in Figure 7. In both examples, the spectral characteristics described above are reproduced. The variation of the probed spectrum with pump frequency is drawn attention to by the extra lines in the contour plots which mark the positions of the local minima (thick dashed lines) and maxima (thick solid lines) of the transient probe spectra as a function of pump frequency. The peak negative bleach signal tracks the diagonal of the graph for pump frequencies $>1650\text{ cm}^{-1}$. However, when the pump reaches the absorption maximum of the amide I band, the negative bleach signal leaves the diagonal and is pushed to higher frequencies. The peak position of the excited-state absorption band, on the other hand, stays more constant (between 1620 and 1640 cm^{-1}). The double peak structure which shows up when pumping the very low-frequency edge of the band is drawn attention to in Figure 8a,b by branching lines.

The 2D-IR spectra of apamin and scyllatoxin are similar in their overall characteristics. However, they differ in some details. Most pronounced is the fact that the negative band is sharper in apamin than the corresponding band in scyllatoxin. The positive band, on the other hand, appears sharper in scyllatoxin. In addition, the spectral splitting observed when pumping at the low-frequency side of the amide I band is more pronounced in apamin.

4. Discussion

4.1. Transient Pump–Probe Spectra. In what follows, a model describing a coupled vibrational system is developed. The model is static in that it does not incorporate vibrational relaxation and vibrational energy redistribution pathways. Its purpose is to provide a framework for describing the transient difference spectra of the broad band and narrow band pump experiments immediately after vibrational excitation before relaxation mechanisms change the initial population distribution.

4.1.1. Excitonic Model. The model is based on the result found by Krimm et al. who, in their normal mode calculations, showed that the dominant coupling mechanism between different peptide units is a through space transition dipole interaction.¹

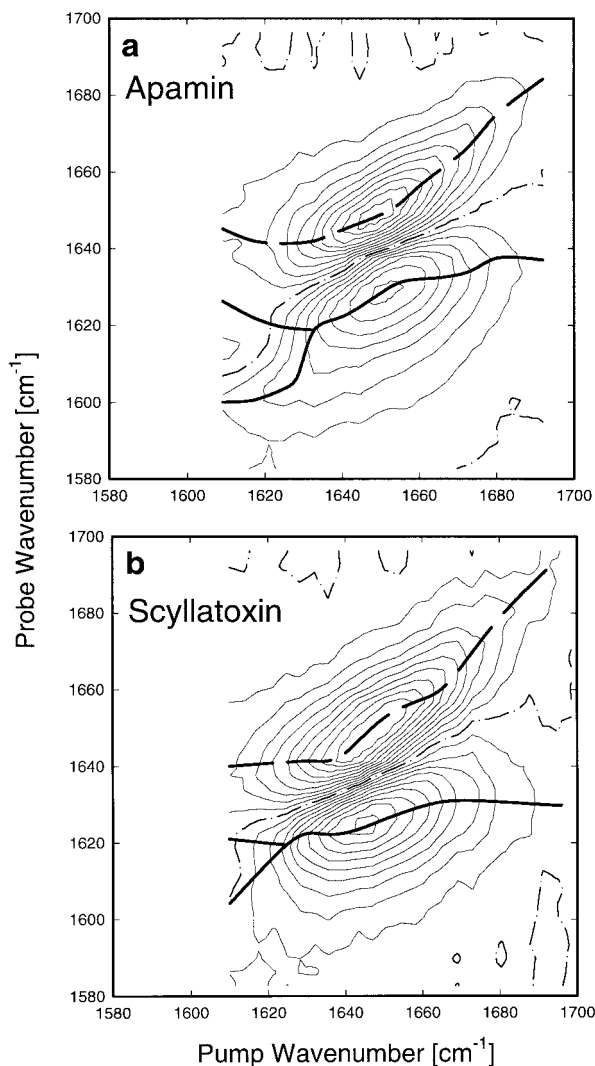


Figure 8. 2D-IR pump-probe spectra of apamin and scyllatoxin shown as contour plots. The spectra are constructed by plotting the spectral response of the sample as a function of the peak position of the narrow band pump pulse. The spectral width of the pump pulses was 14 cm^{-1} in this experiment, and the delay time was set to zero. The isosbestic line is marked by a dashed-dotted line. The thick lines mark the position of the local maxima (thick solid lines) and minima (thick broken line) of the probe spectra as a function of the pump frequency.

Recently, Tasumi et al.^{8,9} considered the amide I band as an excitonic band where the individual monomeric peptide groups are coupled by only this interaction in analogy to the treatment of electronic molecular excitons.^{10,35} Since the TDC interaction is a function of distances and angles between each pair of peptide groups, this model directly addresses the relationship between tertiary structure of the peptide backbone and the absorption spectrum of the amide I band. The parameters of the model are the vibrational frequency of the monomeric peptide unit, its dipole strength, and the direction and location of the dipole with respect to the peptide group. This approximate normal mode calculation reduces the problem to the amide I vibrational subspace, thereby completely neglecting all the other vibrational modes. This was justified by the frequency separation of the amide I mode from all other modes.³⁶ A good agreement was obtained for the absorption spectra of a number of midsize proteins when the diagonal constants and the location of the dipoles were treated as adjustable parameters in the calculations. Because of its simplicity, we use the approach of Tasumi et al. as a reasonable starting point for describing the nonlinear pump-probe spectra.

To describe the exciton system, the eigenstates of $H = H_0 + V - E_0$ are needed, where H_0 describes the n noninteracting (monomeric) peptide groups

$$H_0 = \sum_{i=1}^n H_i \quad (4.1a)$$

V is the interpeptide potential,

$$V = \sum_{i < j} V_{ij} \quad (4.1b)$$

and E_0 is the ground-state energy which is defined as the origin of the energy scale. Whether the coupling term V consists only of dipole-dipole coupling (as proposed by Tasumi et al.⁸) or includes additional terms such as kinematic coupling (as implicitly considered in the normal mode calculations performed by Krim et al.¹), or higher multipole interactions³⁷ is not vital to the following discussion.

The diagonalization is readily accomplished in the basis of site excitations involving 0,1,2 quanta: $|0\rangle$; $\{|i_1\rangle\} = \{|0_0, 1_0, 2_0, \dots, i_1, \dots, n_0\rangle\}$; $\{|i_1j_1\rangle\}$; and $\{|i_2\rangle\}$. The ground state is $|0\rangle$, having no vibrational quanta excited. The $\{|i_1\rangle\}$ have one vibrational quantum on the i th site, and the $\{|i_1j_1\rangle\}$ are two-particle states having one quantum on each of the i th and the j th site. The $\{|i_2\rangle\}$ correspond to two quanta on the i th site. The matrix elements of H are readily obtained as

$$\langle 0|H|0\rangle \equiv 0 \quad (4.2a)$$

$$\langle i_1|H|i_1\rangle = \epsilon_i + \Delta D_1^{(i)} = \omega_e^{(i)} - \Delta + \Delta D_1^{(i)} \quad (4.2b)$$

$$\langle i_1|H|j_1\rangle = \beta_{ij} \quad (4.2c)$$

$$\langle i_1j_1|H|i_1j_1\rangle = (\epsilon_i + \epsilon_j) + \Delta D_{11}^{(i,j)} = \omega_e^{(i)} + \omega_e^{(j)} - 2\Delta + \Delta D_{11}^{(i,j)} \quad (4.2d)$$

$$\langle i_2|H|i_2\rangle = 2\epsilon_i - \Delta + \Delta D_2^{(i)} = 2\omega_e^{(i)} - 3\Delta + \Delta D_2^{(i)} \quad (4.2e)$$

$$\langle i_1j_1|H|i_1k_1\rangle = \beta_{jk} \quad (4.2f)$$

$$\langle i_1j_1|H|i_1j_1\rangle = \sqrt{2}\beta_{ij} \quad (4.2g)$$

The fundamental vibrational frequency of the i th site is $\epsilon_i = \omega_e^{(i)} - \Delta$ and its first overtone frequency is $2\omega_e^{(i)} - 3\Delta$, where Δ is the anharmonic shift. The resonance coupling is β_{ij} , and in eq 4.2g a harmonic oscillator assumption and dipole approximation for V was made. The ΔD terms correspond to the shifts of the monomer frequency that occur on peptide formation. In general, all these terms are different. Even different sites may have different shift terms because of the lack of a symmetry in the peptide. In the following it is assumed that $\Delta D_{11}^{(i,j)} = \Delta D_1^{(i)} + \Delta D_1^{(j)} = 2\Delta D_1^{(i)}$ (see Figure 9 for an illustration with three levels). This approximation ensures that the coupled system is still harmonic in first order (i.e. when $\Delta = 0$). In the model calculations, both the effective fundamental frequency $\epsilon_i + \Delta D_1^{(i)}$ and effective anharmonicity $\Delta' = \Delta - (\Delta D_2^{(i)} - \Delta D_{11}^{(i,j)})$ are treated as parameters. All sites are assumed to have the same Δ' .

In the basis of site excitations, the Hamiltonian H decouples into separate blocks when assuming that V_{ij} is bilinear in the coordinates of site i and j . The blocks represent states with 0, 1, or 2 vibrational quanta, respectively (the number of total vibrational quanta is a good quantum number of H). The matrix

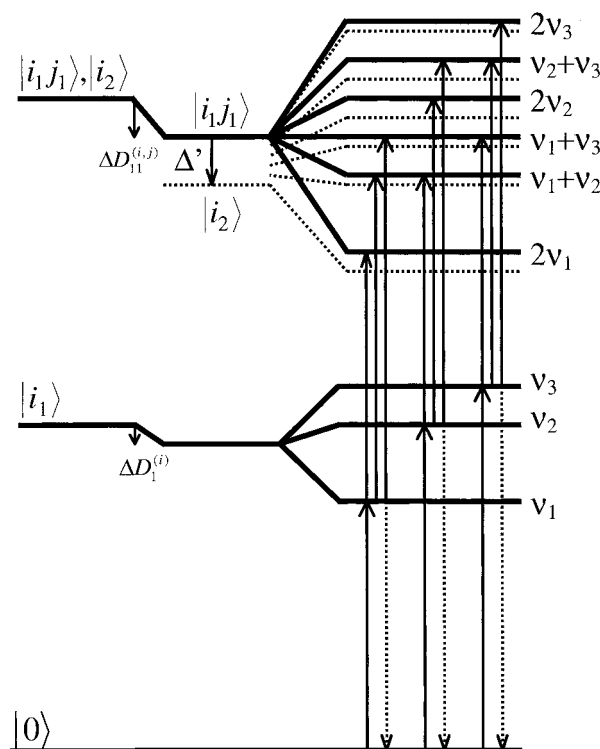


Figure 9. Coupling scheme demonstrating the one-exciton and the two-exciton band of a hypothetical peptide with three peptide groups. $|0\rangle$ denotes the ground state, $|i_1\rangle$ a single excitation on the monomeric peptide site i , $|i_1j_1\rangle$, $i \neq j$, two single excitations on different sites i and j , and $|i_2\rangle$ a double excitation on site i . The resulting coupled excitonic states are numbered $v_1 - v_3$. When assuming that the monomeric states are harmonic (anharmonicity $\Delta = 0$), the energies of the two-excitonic states are sums of the energies of the one-excitonic states and transitions as depicted by the arrows are dipole allowed. When anharmonicity is introduced, all one-exciton \rightarrow two-exciton transitions are frequency shifted (dotted lines).

representing the one exciton (eqs 4.2b,c) has the dimensions $n \times n$ (where n is the number of peptide groups) and the matrix representing the two excitons (eqs 4.2d,g) has the dimensions $n(n+1)/2 \times n(n+1)/2$, respectively.

Two important points arise in the present case that are not encountered in common applications of electronic molecular excitons: (i) All transitions between the ground and one-exciton states potentially have oscillator strength since even the average structure of a peptide does not have any symmetry. (ii) The states $|i_1j_1\rangle$ and $|i_2\rangle$ are almost degenerate, and consequently double excitations on one site are possible and the fermion-like character of weakly excited molecular excitons is not valid.

Useful physical insight regarding the one-exciton \rightarrow two-exciton transitions is obtained by first considering that the monomeric states are harmonic with $\Delta' = 0$. In this case, the system of linearly coupled harmonic oscillators is again harmonic and the resulting eigenstates are completely decoupled from each other. Thus, in this case, the two-exciton states are known directly when the one-excitonic states are known, without explicitly diagonalizing the two-exciton matrix: Their energies are sums of the energies of the one-excitonic states, and the transitions that are possible are depicted in Figure 9. *However, in this case one expects a difference signal which is exactly zero in a pump probe experiment.* This is a consequence of the properties of a harmonic oscillator. As discussed above, when population is moved to the one-quantum (one-exciton) region, three transitions contribute to the pump probe signal: the depleted ground-state absorption $0 \rightarrow 1$; the stimulated

emission $1 \rightarrow 0$ which has the same intensity, direction, and frequency as the bleach; and the excited-state absorption $1 \rightarrow 2$ which has twice the intensity, positive sign, and the same frequency as the previous contributions. The sum of these three contributions is zero for a harmonic system.

When $\Delta \neq 0$, the monomeric states $|i_1j_1\rangle$ and $|i_2\rangle$ are split and anharmonicity is introduced into all one-exciton \rightarrow two-excitonic transitions. Not only those transitions which doubly excite a one exciton (for example the $v_1 \rightarrow 2v_1$ transition in Figure 9) are frequency shifted, but also transitions such as $v_1 \rightarrow v_1 + v_3$ will not have the same frequency as the transition from the ground state to v_3 . Transitions which are forbidden in the harmonic approximation (for example $v_1 \rightarrow v_2 + v_3$) become weakly allowed. In other words, Δ introduces not only diagonal but also off-diagonal anharmonicity. The detailed anharmonic shifts depend on the coupling Hamiltonian which is determined by the tertiary structure of the peptide.

The average anharmonic shift of the two-excitonic states can be easily calculated: Since the average energy of all states is conserved by the coupling term V and since there are $n(n-1)/2$ states of the form $|i_1j_1\rangle$ and n states of the form $|i_2\rangle$ (which are downshifted by Δ), the average anharmonic shift of the excitonic states is $2\Delta/(n+1)$. It decreases reciprocally with the number n of coupled oscillators.

Model calculations of the spectrum were performed for apamin and scyllatoxin.³⁸ In these cases, the peptide structure has been determined by NMR spectroscopy.¹⁴⁻¹⁶ For scyllatoxin, the Brookhaven Protein Data Bank entry 1SCY was used.^{16,39,40} The structure data of apamin is not listed in the Brookhaven Protein Data Bank and were obtained directly from the authors of ref 14. The transition dipole-dipole coupling constants (i.e. the off-diagonal elements of the Hamiltonian) are calculated according to

$$\beta_{ij} = \frac{\vec{\mu}_i \cdot \vec{\mu}_j - 3(\vec{n}_{ij} \cdot \vec{\mu}_i)(\vec{n}_{ij} \cdot \vec{\mu}_j)}{r_{ij}^3} \quad (4.3)$$

where the \vec{n}_{ij} are the unit vectors of vectors connecting two sites \vec{r}_{ij} . The magnitude of the transition dipole moments (0.37 D) and the direction and effective location of the individual point transition dipoles with respect to the peptide group³⁷ were obtained from ref 8. For a perfectly symmetric α -helix these parameters result in two dominating interaction terms which are those between nearest neighbors ($\beta_{i,i+1} \approx +15 \text{ cm}^{-1}$) and those between the third nearest neighbors which correspond to one complete helix turn ($\beta_{i,i+3} \approx -7 \text{ cm}^{-1}$).

When the oxygen of a particular peptide group is not hydrogen bonded, the monomeric amide I frequencies (i.e. the diagonal constants of the one-exciton Hamiltonian) were chosen as $\epsilon_i = 1655 \text{ cm}^{-1}$. This value was determined such that the peak position of the calculated linear absorption spectrum of scyllatoxin matches the actual peak position. It is well-established that hydrogen bonding causes a red shift of the monomeric frequency.^{2,5,41} This is seen, for example, in the difference between the peak position of the linear absorption spectrum of NMAD in D_2O and $\text{DMSO}-d_6$ which does not form hydrogen bonds. When the oxygen of a peptide group is hydrogen bonded, the monomeric amide I frequency ϵ_i is frequency shifted from 1655 cm^{-1} by a value $\Delta\epsilon_i$ which is linearly dependent on the O...H distance (r_{OH} , given in angstroms):

$$\Delta\epsilon_i = \alpha_{\text{Hvd}}(2.6 - r_{\text{OH}}) \quad (4.4)$$

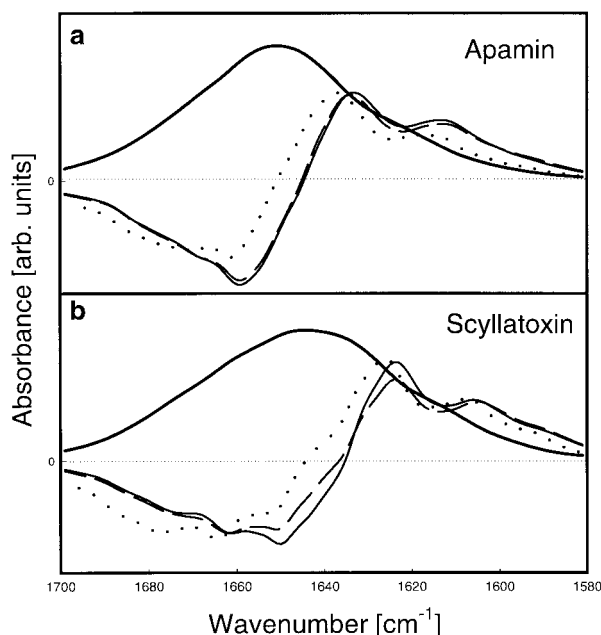


Figure 10. Model calculation of the linear absorption spectrum (thick solid line) and its first derivative (dotted line) and the difference spectrum obtained in a broad band pump experiment (solid line, before equilibration; dashed lines, after equilibration) of apamin and scyllatoxin. A diagonal disorder of $\Delta\omega_{\text{dia}} = 24 \text{ cm}^{-1}$ (2σ interval) and a hydrogen bond shift of $\alpha_{\text{Hbd}} = -30 \text{ cm}^{-1}/\text{\AA}$ is assumed in these calculations. The model spectra can be directly compared to the corresponding experimental results in Figure 1a,b and Figure 6a,b.

where the constant α_{Hbd} is normally chosen as $-30 \text{ cm}^{-1}/\text{\AA}$ which results in a frequency downshift of $\approx 20 \text{ cm}^{-1}$ for a typical hydrogen bond length of $1.9\text{--}2.0 \text{ \AA}$ and gives a good agreement between the model 2D-IR pump probe spectra and the experimental results. A frequency downshift of this order was obtained recently by ab initio calculations⁴¹ but is smaller than that assumed in ref 2. The value $\Delta = 16 \text{ cm}^{-1}$, deduced from the measurement on NMAD in DMSO- d_6 , was used for the anharmonicity.

NMR structure data files contain more than one structure (25 structures in the case of scyllatoxin and 6 in the case of apamin), all of which conform with the NMR spectrum and which commonly are energy minimized. These structures represent a realistic subset of possible conformers. Averaging over spectra calculated for each of these structures is one way to account for the structural inhomogeneities responsible for spectral broadening of the amide I band. Since a point dipole approximation was used for V , it was straightforward to use these structures to account for the disorder in the off-diagonal coupling elements β_{ij} . A similar treatment for the disorder in the diagonal energies ϵ_i is much more involved and would require quantum chemical calculations. Therefore, the diagonal disorder was modeled by an uncorrelated random Gaussian distribution, and the standard deviation $\Delta\omega_{\text{dia}}/2$ of this distribution was treated as a variable parameter. The disorder of the two-exciton states was chosen to be strictly correlated to that of the one-exciton states in accordance with eqs 4.2d,e,g. Averaging was performed in the following way: For each individual structure, a set of spectra was calculated from various choices (conformers) of random diagonal disorder. This was repeated for all available structures, and the final spectra were calculated by averaging over all these conformers. Typically 250 conformers were used to obtain the spectra shown in Figures 10–12.

In the following description of the pump–probe spectra, it is assumed that the initially prepared coherent superposition of

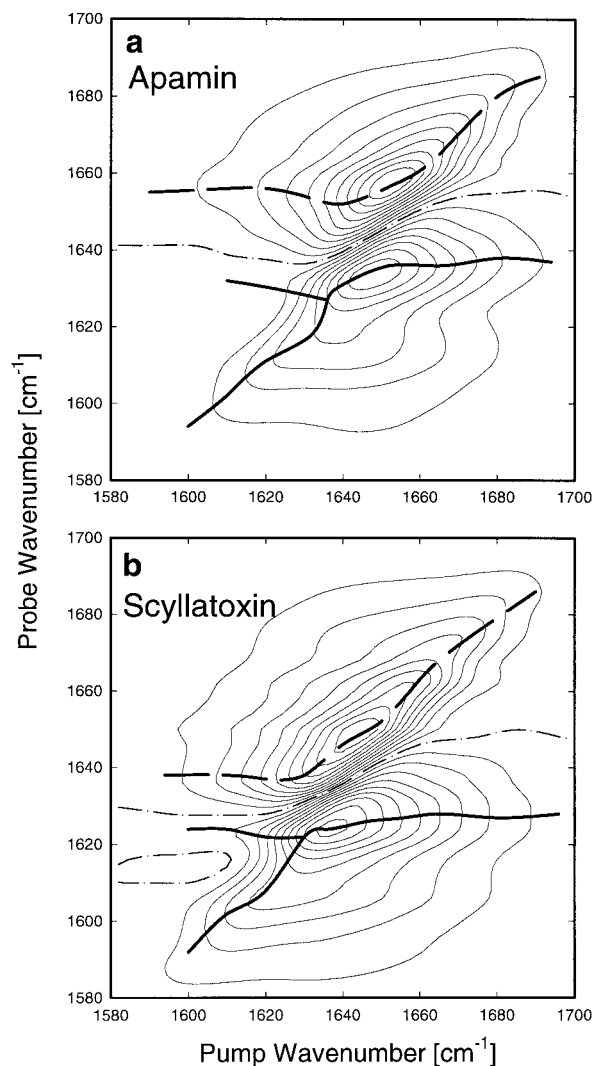


Figure 11. Simulated 2D-IR pump–probe spectrum of apamin and scyllatoxin as contour plots. This model calculation can be directly compared with the experimental results of Figure 8. A diagonal disorder of 24 cm^{-1} (2σ interval), a hydrogen bond shift of $\alpha_{\text{Hbd}} = -30 \text{ cm}^{-1}/\text{\AA}$ and a spectral width of the pump pulse of 12 cm^{-1} was assumed for this set of calculations. The isosbestic line is marked by dashed–dotted line. The thick solid lines mark the position of the local maxima (thick solid line) and minima (thick broken line) of the probe spectra as a function of the pump frequency.

one-exciton states has dephased on a time scale given by the total inverse bandwidth of the amide I band (see sections 3.2 and 4.2.1). After a delay time $> 400 \text{ fs}$, only the diagonal elements of the density matrix contribute to the pump–probe spectra and the incoherent description given below is valid.

The pump pulse, which has a spectrum $I(\omega)$, places a relative population n_k into each of the one-exciton states k , where n_k is a convolution of the spectrum of the pump pulse and the absorption spectrum of the transition:

$$n_k = \frac{1}{2\pi} \int I(\omega) |\bar{\mu}_{g,k}|^2 \frac{\gamma}{(\omega - \omega_{g,k})^2 + \gamma^2/4} d\omega \quad (4.5)$$

The ground-state population is thereby reduced by $\delta n = \sum_k n_k$, and the bleach spectrum is given by

$$\Delta A_B = -\delta n S_g(\omega) \quad (4.6)$$

where $S_g(\omega)$ is the conventional ground-state spectrum:

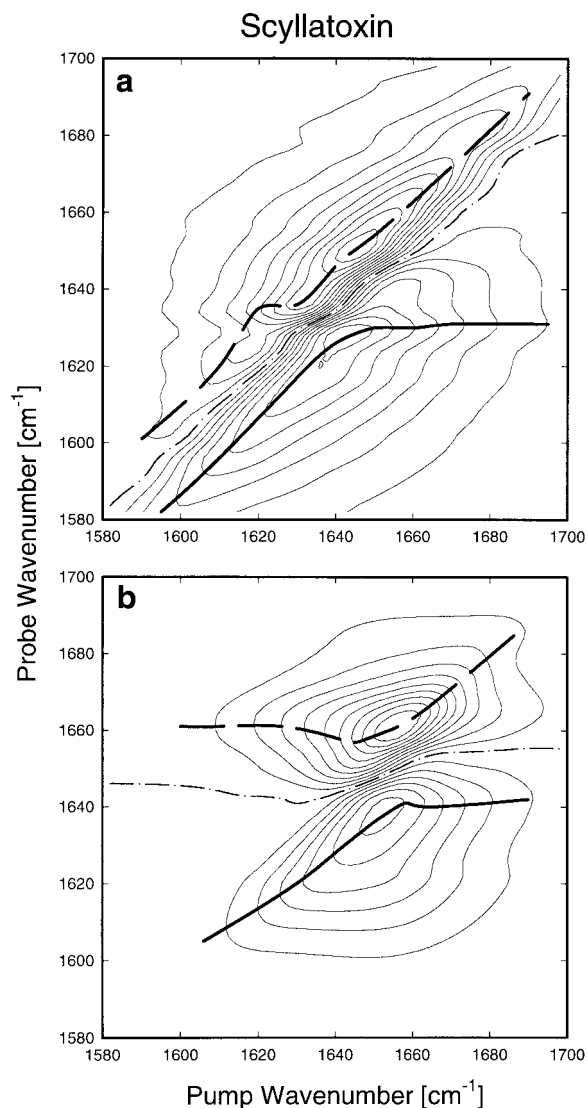


Figure 12. Dependence of the 2D-IR pump-probe spectrum on model parameters, demonstrated here for scyllatoxin. In the upper graph (a), the diagonal disorder is increased to 50 cm^{-1} (2σ interval) and all other parameters are the same as in Figure 11. In the bottom graph (b), the hydrogen bond dependent frequency shift is ignored ($\alpha_{\text{Hyl}} = 0$) and all other parameters are unchanged. The isosbestic line is marked by a dashed-dotted line. The thick solid lines mark the position of the local maxima (thick solid line) and minima (thick broken line) of the probe spectrum as a function of the pump frequency.

$$S_g(\omega) = \sum_k |\bar{\mu}_{g,k}|^2 \frac{\gamma}{(\omega - \omega_{g,k})^2 + \gamma^2/4} \quad (4.7)$$

The stimulated emission contribution to the difference spectrum is given by

$$\Delta A_{\text{SE}} = - \sum_k n_k |\bar{\mu}_{g,k}|^2 \frac{\gamma}{(\omega - \omega_{g,k})^2 + \gamma^2/4} \quad (4.8)$$

Finally, the one-exciton \rightarrow two-exciton spectrum is

$$\Delta A_{12} = \sum_{k,p} n_k |\bar{\mu}_{k,p}|^2 \frac{\gamma}{(\omega - \omega_{k,p})^2 + \gamma^2/4} \quad (4.9)$$

and the total difference spectrum is the sum of these contributions: $\Delta A = \Delta A_B + \Delta A_{\text{SE}} + \Delta A_{12}$.

The one-exciton states $\{|k\rangle\}$ and the two-exciton states $\{|p\rangle\}$ are known from the matrix diagonalization, the transition dipoles are obtained in the harmonic approximation, $\bar{\mu}_{12} = \sqrt{2}\bar{\mu}_{01}$, and the $0 \rightarrow 2$ transitions are assumed to have negligible transition moments, $\bar{\mu}_{02} = 0$. A value of 10 cm^{-1} is assumed for γ which corresponds to the full homogeneous bandwidth of the individual transitions. A justification for the choice of this value is given in section 4.2.3.

The spectral intensity of the pump pulse $I(\omega)$ is modeled by a constant function when simulating the broad band pump experiment (δ -pump) or a Lorentzian function with a full width of 12 cm^{-1} when simulating the narrow band pump experiment, respectively. Expressions 4.5–4.9 reflect the situation *before* population equilibration between different eigenstates has taken place. The pump-probe spectra for the case of complete equilibration between all states is calculated from expressions similar to 4.5–4.9 but with n_k equal to a constant.

4.1.2. Results and Comparison with the Experiment. Figure 10 shows simulated absorption spectra, their first derivative (dotted line), and the broad band pump-probe-difference spectra (solid line, before equilibration; dashed lines, after equilibration) of apamin and scyllatoxin. These plots are to be compared with the corresponding experimental data of Figure 1a,b and Figure 6a,b. Shown in Figure 11 are simulated 2D-IR pump-probe spectra of apamin and scyllatoxin which are to be compared with experimental results of Figure 8. In Figures 10 and 11, the diagonal disorder $\Delta\omega_{\text{dia}} = 24 \text{ cm}^{-1}$ (two times the standard deviation of the Gaussian diagonal disorder) and the hydrogen bond dependent frequency shift $\alpha_{\text{Hyl}} = -30 \text{ cm}^{-1}/\text{\AA}$ were determined by finding the best fit between experimental and modeled spectra. It will be seen below that the 2D-IR spectra are much more sensitive to the model parameters than the broad band pump spectra. The overall agreement between the model and experiment is excellent. Some important points will now be discussed in more detail.

The shift between the zero crossing of the first derivative of the absorption spectrum and the early transient difference spectra (i.e. the experimental 400 fs spectra in Figure 6 and the nonequilibrated modeled spectra in Figure 10) is almost exactly reproduced by the calculations. This shift is sensitive to the anharmonicity Δ in the model calculation, but the used NMAD value of $\Delta = 16 \text{ cm}^{-1}$ predicts the correct shift.

The broad band pump spectra are very insensitive to equilibration, as can be seen from the minor differences between nonequilibrated and equilibrated spectra in Figure 10. This is due to the fact that the broad band pump tends to smear out the spectrum because of the overlapping contribution from the different eigenstates. The significant changes seen in experimental difference spectra at early (400 fs) and later (2.4 ps) times cannot be accounted for by equilibration. The experimentally observed shift between the 400 fs spectrum and the 2.4 ps one must indicate that vibrational relaxation (which is not part of the simple model) is faster for states on the low-frequency side of the amide I band. Independent evidence for this interpretation comes from the excitation frequency dependent decay rate of the hole in the narrow band pump experiment (Figure 7).

The agreement between the experimental and the calculated 2D-IR spectra is excellent. All spectral features described in the Experimental Section are reproduced, in particular the dependence of the position of the hole and the dependence of the width and position of the excited-state absorption on the pump frequency. *These results are a direct manifestation of delocalization of vibrational excitons.* Mixing of the anhar-

monicity Δ into all possible one-exciton \rightarrow two-exciton transitions is an essential part of the modeling. If the states were localized on single peptide units one, would observe an anharmonic frequency shift which is essentially the same for all states and which is not frequency dependent, in significant contrast to the experimental results. The model parameters that tend to localize the amide I states are the diagonal disorder $\Delta\omega_{\text{dia}}$ and the hydrogen bond dependent frequency shift α_{Hyd} . In Figure 11, both parameters are determined ($\Delta\omega_{\text{dia}} = 24 \text{ cm}^{-1}$, $\alpha_{\text{Hyd}} = -30 \text{ cm}^{-1}/\text{\AA}$) by finding the best fit between experimental and modeled spectra. The dependence of the 2D-IR spectrum on diagonal disorder is demonstrated in Figure 12a, which shows a simulation of the 2D-IR pump-probe spectrum of scyllatoxin where the diagonal disorder $\Delta\omega_{\text{dia}}$ is increased to 50 cm^{-1} and all other parameters are unchanged. Stronger localization of the states manifests is now seen in the 2D-IR pump-probe spectrum from the location of the bleach and excited-state absorption signals, which have become close to the diagonal of the graph over the whole frequency range.

The double peak structure obtained when pumping the very low-frequency edge of the amide I band is also reproduced by the model calculations. The calculations show that it is the hydrogen bond dependent frequency shift that causes this spectral feature. This is demonstrated in Figure 12b, which shows a 2D-IR pump-probe spectrum of scyllatoxin with all parameters unchanged except that the hydrogen bond dependent frequency shift α_{Hyd} is set to zero. The double peak structure is clearly missing in this simulation. The two peaks arise because the peptide has two zero-order vibrational frequencies separated by ca. 20 cm^{-1} : one from peptide groups which are hydrogen bonded and another from those that are not. Interestingly, this splitting is not apparent in the linear absorption spectrum.

Also some of the differences in the shape of the negative and the positive bands of the apamin and the scyllatoxin spectra, such as the sharper peak in the excited-state absorption of scyllatoxin, are reproduced by the model calculation.

4.1.3. Delocalization. There are a number of useful measures of delocalization, each of which has a different meaning. One is the geometric size of the excitonic wave functions, a measure of which is the quantum connectedness length ξ ,⁴² defined as

$$\xi^2 = \frac{\sum_{ij} \langle \Delta_{ij} \rangle r_{ij}^2}{\sum_{ij} \langle \Delta_{ij} \rangle} \quad (4.10)$$

where r_{ij} is the distance between sites i and j and Δ_{ij} is the quantum connectivity of these sites, given by $\Delta_{ij} = R_{ij}(R_{ii}R_{jj})^{-1/2}$ with $R_{ij} = \sum_k a_{ki}^{-2} a_{kj}^2$. The a_{ki} are the coefficients of the wave function of state k on site i and the average $\langle \dots \rangle$ is taken over the distribution of conformers which were used to calculate the averaged spectra. A delocalization over a distance of $\xi = 8 \text{ \AA}$ is found for scyllatoxin, using the model parameters from the best fit of the spectra of Figures 10 and 11.

Another measure of delocalization is the number of units, P_ρ , over which the excitation is delocalized in terms of the density matrix:^{43,44}

$$P_\rho = \frac{(\sum_{ij} |\langle \rho_{ij} \rangle|)^2}{n \sum_{ij} |\langle \rho_{ij} \rangle|^2} \quad (4.11)$$

where the density matrix elements are in the site basis and the average $\langle \dots \rangle$ is taken over all conformers. The relevant density matrix depends on the way in which the one-exciton states are prepared and measured. Mukamel et al. used a thermal distribution in the case of the photosynthetic antenna complex, assuming that equilibration between the eigenstates is fast compared with the measurement process.⁴³ However, in the case of the peptide, it was shown experimentally that equilibration is relatively slow, and consequently, we have to take into account the preparation of the density matrix by the pump pulse. If all states were excited equally, the result would be $P_\rho = 1$. The largest possible delocalization is obtained when selectively exciting only a few eigenstates, as has been done in the narrow band pump experiment. We find $P_\rho = 7.2$ for scyllatoxin when assuming the pump pulse is centered at the peak of the absorption band (1645 cm^{-1}) and has a bandwidth of 10 cm^{-1} . It was assumed that the off-diagonal elements of the density matrix in the eigenstate basis have been decayed. The value of P_ρ slightly depends on the pump pulse frequency. For example, it is $P_\rho = 6.0$ at the high-frequency side of the amide I band (1680 cm^{-1}).

Another commonly used measure of delocalization is the participation ratio P_k .⁴⁴⁻⁴⁶

$$P_k = \langle (\sum_i a_{ki}^4) \rangle^{-1} \quad (4.12)$$

The participation ratio is defined for each individual excitonic state k . We have calculated the average over all states $P = (1/n) \sum_k P_k$, since in the case of a peptide none of the excitonic state is somehow unique as would be the case for aggregates with high symmetry. For scyllatoxin a value of $P = 4.1$ is obtained.

When a larger diagonal disorder of 50 cm^{-1} is used, all the above measures indicate stronger localization. However, the delocalization parameters showed different sensitivity to disorder. For example, the quantum connectedness length is reduced only by ca. 10% while the other measures are reduced by ca. 30%. Comparison with the model calculations show that this amount of disorder is enough to mostly remove the delocalized character of the 2D-IR pump-probe spectrum (see Figure 12a). Apparently, the participation ratios P and P_ρ more effectively represent the strong dependence of the 2D-IR pump-probe spectrum on disorder.

According to the previous estimate, vibrational energy could be transferred over a range of ca. 8 \AA , which is the effective size of the vibrational excitation. However, the range of this transport is further limited by the vibrational energy relaxation which occurs on a 1 ps time scale. In a one-dimensional representation of the α -helix the peak group velocity of an excitonic wave packet is estimated as $v_{\text{gr,max}} = 4\pi\beta = 6$ amino acids/ps for a nearest neighbor coupling of $\beta_{i,i+1} = 15 \text{ cm}^{-1}$. When transport along the line of the hydrogen bonds is assumed ($\beta_{i,i+3} = -7 \text{ cm}^{-1}$, 3 amino acids/turn), a somewhat larger velocity of 8 amino acids/ps is estimated. This corresponds to ca. 2 α -helix turns or a distance of ca. 12 \AA , respectively. Therefore, the range estimated by the measures of delocalization is similar to the distance a wave packet could be transported, and the coherent delocalization of the state is not significantly limited by the lifetime.

It has been proposed in the literature that coherent transport of vibrational energy along an α -helix would optimize the efficiency of enzyme reactions in biological systems. This was first suggested by Davydov^{47,48} and is known as Davydov's

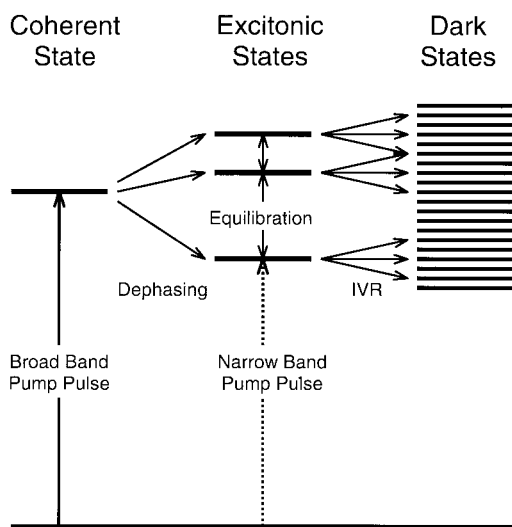


Figure 13. Scheme indicating possible relaxation processes after pumping an excitonic system. Since the broad band pump pulse covers all excitonic states, it excites a coherent superposition which will dephase very rapidly on a time scale given by the width of the distribution of states. Subsequently, the initial population distribution of the excitonic states will be changed by population equilibration and by energy transfer to dark intramolecular states (IVR) or solvent states. The narrow band pump pulses, on the other hand, are longer than the dephasing time of the excitonic states and therefore directly excite the stationary excitonic states without the initial dephasing step.

soliton. Our results indicate that coherent transport will not occur over more than 8 Å.

4.2. Relaxation Processes. The spectral simulations of section 4.1. are entirely static and as such are only intended to rationalize the transient difference spectra before relaxation processes change the initial population distribution. It was demonstrated that the model reproduces the shape of the early time difference spectra very well. However, the spectrum is changing with time because the system is undergoing vibrational relaxation and vibrational energy migration.

In the broad band pump–probe experiment, one would expect to observe three relaxation processes on three different time scales: (i) Dephasing of the initially prepared pure state, which is a coherent superposition of the stationary excitonic states encompassed by the ultrashort pump pulse spectrum; (ii) vibrational energy relaxation due to intramolecular energy redistribution (IVR) or possibly also due to direct energy transfer into the solvent; and (iii) population equilibration between the stationary excitonic states. These relaxation processes are shown schematically in Figure 13 and will be discussed in the following sections.

In the narrow band experiment, on the other hand, the pump pulses are longer than the dephasing time of the stationary states, as seen in the bandwidth of the hole in the hole burning experiment which is broader than the bandwidth of the pump pulse (see Figure 7b). In this case, one can assume that the quasi-stationary eigenstates are excited directly without the initial dephasing step, as shown in Figure 13.

4.2.1. Dephasing. The spectral width of the pump pulses encompasses all stationary amide I states (i.e. all eigenstates). Since the pump pulses are almost transform limited, they are short enough to excite a coherent superposition of these states. However, since the frequencies of the stationary states are different, the initial phase relation is destroyed quickly on a time scale which is related to the total spectral width of the amide I band.⁴⁹

This dephasing process can be manifested in the magic angle pump–probe and in the anisotropy signal since the dipole moment of the coherent superposition state in general will be different from the sum of dipole moments of the individual states. However, the dephasing process will be more evident in the anisotropy signal since the anisotropy is particularly sensitive to changes in the direction of the total dipole moment and it is known that interference between different transitions can modify the anisotropy significantly.⁵⁰

Experimentally, an initial fast decay is indeed observed in both signals. The time constant of this fast component is roughly the same in both cases, and its value (ca. 300 fs) fits very well to the inverse bandwidth of amide I band (30–40 cm^{-1}). As expected, the faster component is dominating the anisotropy signal ($a_1/a_2 > 2$) but is relatively small in the magic angle pump–probe signal ($a_1/a_2 \approx 0.6$). Strong support for this interpretation for the initial decay comes from the observation that no such fast decay is found in the anisotropy of NMAD. In that case, only one dipole allowed vibrational transition is involved and no interference of this type is possible.

A more quantitative interpretation than this is complicated by the fact that the bleach, the stimulated emission, and the excited state absorption all contribute differently to the magic angle pump–probe signal and to the anisotropy signals and they spectrally overlap significantly. Thus, at this stage, we can provide only a qualitative description of the dephasing process.

4.2.2. Vibrational Relaxation. The slower time constant in the magic angle pump–probe signal of the peptide samples (1.2 ps) is assigned to vibrational population relaxation which occurs on roughly the same time scale in all investigated peptides. In NMAD vibrational relaxation is even faster. For this case, the fast component in the pump–probe signal (450 fs) must reflect vibrational relaxation (and not the initial dephasing process as observed in the peptide) since no interference signal has been observed in the anisotropy signal. Nevertheless, essentially the same ultrafast time scale is observed for vibrational relaxation of the amide I mode of all samples, and we conclude that this is an intrinsic property of the peptide group itself and does not reflect a specific characteristic of the surroundings of the peptide bond.

The time scale is too fast to be explained by direct energy transfer between the amide I mode and the solvent or surroundings of the peptide group. Such a relaxation would be expected to occur in 10–100 ps (see ref 51 for a review on typical vibrational relaxation rates). For example, vibrational relaxation of the aqueous CN^- ion, which has a comparable frequency, occurs in 30 ps in H_2O ²³ even though the strong Coulomb interaction between the ion and water assists relaxation.⁵² Therefore, vibrational relaxation of the amide I mode is suggested to be the result of intramolecular energy redistribution (IVR). IVR has been extensively studied, and a summary is given in a number of review articles.^{51,53–55} Most work has been done for C–H stretching modes where, in particular, the work by Kaiser et al.^{53,55,56} demonstrated the important effect of Fermi resonances. Vibrational relaxation of C–H-stretching modes in general is ultrafast (1 ps) because of strong anharmonic coupling to the first overtone of the C–H bend mode and the large density of states at ca. 3000 cm^{-1} in the molecules that were studied. Much less work has been done in a lower frequency regime or for C=O groups in particular. The T_1 time of acetylbromide ($\text{CH}_3\text{BrC=O}$) in CCl_4 was reported to be 10 ps.⁵⁷ Carbon oxygen triple bonded systems have long relaxation times: 20 ps for the CO stretch for carbon monoxide bonded to the heme iron of myoglobin^{12,13} and hundreds of picoseconds

for metal carbonyls.⁵⁸ Also $\text{C}\equiv\text{C}$ stretching modes relax on a relatively slow time scale of 15–240 ps, again strongly dependent on anharmonic coupling to combination modes.⁵⁹

In terms of this discussion, the observed time constant of 1.2 ps for the peptide and 400 fs for the isolated NMAD molecule has to be considered as extraordinarily fast and is probably the result of specific Fermi resonances, analogous to the mode-specific pathway for the relaxation of C–H stretching modes into C–H bending modes. NMAD is not a very large molecule (12 atoms), and we probably have to deal with the “intermediate coupling situation”, i.e., with a few but strongly coupled modes.^{49,56} Two experimental observations support this conclusion: the biexponential decay of the pump–probe signal of NMAD (0.4 and 4 ps) and the doublet structure in the IR absorption spectrum of NMAD in D_2O . The intermediate coupling situation is understood in a manner identical to that shown in the scheme of Figure 13, yet with a different interpretation of the states. One dipole allowed state shares its oscillator strength with a few nearly resonant anharmonically coupled dark states. The initially excited state is a coherent superposition of all these states and has exactly the same oscillator strength as the uncoupled amide I state. Dephasing of the coherent superposition reduces the oscillator strengths of the amide $\nu = 1 \rightarrow \nu = 2$ and $\nu = 0 \rightarrow \nu = 1$ transition by a factor of N of the original oscillator strength, where N is the number of strongly coupled modes. Subsequently, the signal further decays on a slower time scale due to relaxation of these strongly coupled modes. The anisotropy does not change during this entire process because only one dipole allowed transition is involved in zero order. This is in contrast to the discussion of section 4.2.1 regarding the dephasing of the initially prepared coherence between the exciton states which are composed of n transitions, all of which are dipole allowed and have different dipole directions.

The asymmetric shape of the IR absorption spectrum of NMAD in D_2O supports the interpretation of underlying Fermi resonances. A similar doublet structure has been observed in resonance Raman studies on NMA in H_2O with an even larger splitting of 20 cm^{-1} .⁶⁰ In that case, however, the doublet structure was interpreted in terms of a coupling between the amide I mode and the O–H bending mode of a hydrogen bonded H_2O molecule which are in near resonance. This explanation is unlikely for NMAD in D_2O since in this case the O–D bending frequency is not resonant with the amide I mode.

Regarding the nature of Fermi resonances, possible candidates would be a combination mode of the amide IV band (628 cm^{-1} , essentially the $\text{C}=\text{O}$ bending mode) and the amide III mode (965 cm^{-1} , essentially N–D bending mode), the combination of the amide IV band and a mode found at 1044 cm^{-1} (which involves the $\text{C}=\text{O}$ out-of-plane bend), or the first overtone of a mode found at 872 cm^{-1} (which is a linear combination of the $\text{C}-\text{C}_\alpha$, $\text{N}-\text{C}_\alpha$, and $\text{C}=\text{O}$ stretching mode).^{61,62} This problem might be clarified by studies of isotopomers.

4.2.3. Homogeneous Bandwidth. In a typical hole burning experiment, the width of the hole is given by twice the homogeneous bandwidth, convoluted with the bandwidth of the pump laser. This is true when independent molecules, which lie underneath a broad inhomogeneous distribution, are photobleached.⁶³ However, the determination of the homogeneous bandwidth is more complicated in the present situation since all the $\nu = 0 \rightarrow \nu = 1$ transitions are coupled by the excitonic interaction. Nevertheless, the width of the hole does depend on the homogeneous bandwidth. By fitting the width of the

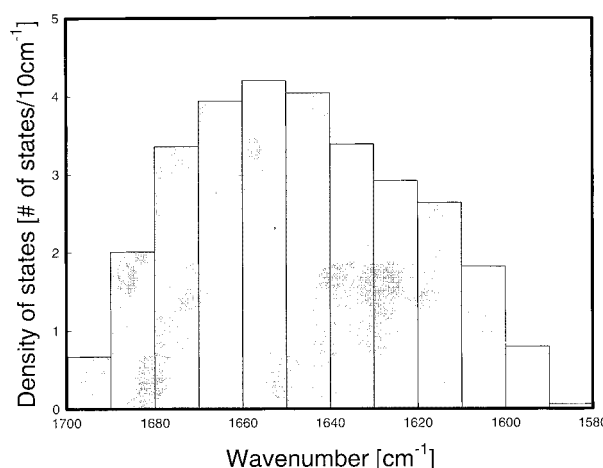


Figure 14. Density of one exciton states within one homogeneous bandwidth (10 ps) shown for the example of scyllatoxin.

hole in the calculated difference spectra to the experimentally observed value (see Figure 7), the homogeneous bandwidth was estimated to be $\gamma = 10\text{ cm}^{-1}$. The lifetime contribution $T_1 = 1.2\text{ ps}$ to the total homogeneous bandwidth is 4.5 cm^{-1} and therefore pure dephasing is approximately $T_2^* = 2\text{ ps}$.

The amide I band consists of as many transitions as there are peptide units. These transitions cover a range of approximately 90 cm^{-1} where the transitions to the middle of the band carry more dipole strength. Additional inhomogeneous broadening, modeled by the diagonal disorder $\Delta\omega_{\text{dia}}$, is relatively small compared with the total width of the distribution of excitonic states. The homogeneous width of each of these $\nu = 0 \rightarrow \nu = 1$ transitions is ca. 10 cm^{-1} . Thus, for a peptide of the size of scyllatoxin (31 amino acids), three to four transitions are found within each homogeneous bandwidth. Other methods, such as low-temperature and photon echo techniques, could be used to suppress or minimize some of this line broadening. However, even in the absence of the inhomogeneous contribution and pure dephasing T_2^* , a significant broadening will still remain because of the short-lifetime T_1 of the amide I vibration. Figure 14 shows the calculated frequency dependence of the density of states for illustration.

4.2.4. Equilibration. The slower time constant observed in the anisotropy decay is considerably slower (2–15 ps) than that found in the pump–probe decay. Two processes potentially can be responsible for the anisotropy decay: rotational diffusion motion of the molecule and equilibration between several nearly resonant states whose transition dipoles have different orientation. Due to the size of the peptide, one expects a much slower time scale of ca. 1 ns for its overall motion. Internal motions, such as low-frequency vibrations, could be faster but would result only in minor changes of the direction of the involved dipoles. The anisotropy of NMAD in D_2O , on the other hand, decays on a 6 ps time scale, which is a reasonable time scale for an overall reorientation of an molecule of this size.

We suggest that the slower process in the anisotropy decay of the peptides is population equilibration between the stationary states. After dephasing of the coherent superposition state (see section 4.2.1), an anisotropy still remains because predominantly those transitions have been excited which are projected maximally onto the pump polarization; thus the immediately formed population is anisotropic. Population equilibration then occurs between all achievable states including those whose transition dipoles are perpendicular to the pump pulse and thus were not excited initially. This process further decreases the anisotropy

signal. On the other hand, the anisotropy is completely insensitive to vibrational relaxation.

This interpretation is supported by the complementarity of the time scales of the anisotropy decay and dynamic hole burning. The dynamic hole burning experiment measures vibrational energy migration more directly than does the anisotropy. It was shown earlier that a broadening of the hole occurs within the first 2.4 ps which is due to population equilibration between adjacent energy states. The time scale of this process is the same as that of the slower phase of the anisotropy signal.

The data show that population equilibration is slower than vibrational relaxation. This is manifested in the width of the hole after 2.4 ps which is still small compared with the total bandwidth of the amide I band. Long before the energy can be equilibrated over all states, the vibrational energy has redistributed into other internal modes. Furthermore vibrational relaxation appears to be faster on the low-frequency side than on the high-frequency side of the amide I band. This was concluded from the faster decay of the hole when it is burned on the low-frequency side and is also consistent with the shift to lower frequencies with time of the isosbestic point of the broad band pump-probe difference spectrum with time. Also, population equilibration is faster on the low-frequency side, as seen in the larger rate of growth of the width of the hole. At this stage, we can only speculate about the reason for this effect. One possibility is that the coupling to the dark states is nonuniform over the investigated spectral bandwidth, possibly being mediated by some specific Fermi resonance, so the excitonic interaction might shift levels into regions where the IVR rate is increased. Another explanation could involve structural inhomogeneity of the relaxation rate. For example, the vibrational frequency of peptide groups which are hydrogen bonded are at lower frequencies, and it is reasonable to assume that hydrogen bonding influences the vibrational relaxation rate.

5. Conclusions

An important result of this work is the evidence that amide I states of proteins are delocalized states. The dependence of the shape of the pump-probe spectrum on the pump wavelength clearly indicates delocalization. A simple excitonic coupling model, incorporating the one-exciton \rightarrow two-exciton transitions, can describe the initial pump-probe spectra almost quantitatively. The calculated spectra critically depend on parameters that cause localization of the vibrational excitations. The assumed diagonal disorder of 24 cm^{-1} is small enough that it does not localize the excitation. On the other hand, no large differences have been found for spectral properties and relaxation mechanisms of three different peptides. This proves that these are very general properties and reflect intrinsic characteristics of small peptides.

The fact that the anharmonicity Δ contributes to all possible transitions suggests an interesting prospect: Even if it were possible to frequency resolve the linear absorption spectrum and to obtain the frequencies and intensities of all one-excitonic states, it would be impossible to uniquely determine the $n(n-1)$ numbers necessary to compose the one-exciton Hamiltonian since only $2n$ measurement values can be obtained. In other words, an unique assignment of the spatial distribution of amide I dipoles, or of the tertiary structure of the peptide, would be impossible. The transition from the one-exciton to the two-excitons, on the other hand, could in principle yield on the order of n^2 observables. Therefore, the complete information necessary to resolve the structure of a peptide is in some respects

hidden within the one-exciton \rightarrow two-exciton transition and might be obtained from nonlinear-infrared spectroscopy.

The experimental 2D-IR spectrum of apamin and scyllatoxin (Figure 8) are indeed slightly different. However, these differences are not great and in particular, the spectra do not resolve into well-separated bands. However, there is in principle sufficient information to build up the complete coupling Hamiltonian. This was demonstrated, for example, by the fact that we were able to distinguish between the localized versus delocalized character of the states, a distinction which is not possible from linear absorption spectra. Furthermore, it was necessary to include a hydrogen bond dependent frequency shift to fit the calculated and observed 2D-IR spectra of the apamin and the scyllatoxin as well as the differences in their spectra. This result indicates that this technique is indeed sensitive to the detailed structure of the coupling Hamiltonian and that the 2D-IR spectra yield more detailed information on the structure of a peptide than can a linear absorption spectrum. It remains to be seen whether this or coherent nonlinear-infrared methods can further expose the detail needed for a method of a structural analysis for peptides. Clearly, studies of smaller model polypeptides are needed.

In conclusion, we have presented the first nonlinear-infrared study of the structure and the femtosecond dynamics of the amide I band of small peptides. The experimental results have permitted us to model this commonly used marker band of peptides and proteins in much more detail than was previously achieved. These experiments have become possible only very recently with the progress in femtosecond laser technology, in particular in the generation of high-power femtosecond IR pulses. This paper also demonstrates that now it is possible to perform femtosecond experiments on coupled vibrational systems in analogy to work on coupled electronic systems.

Acknowledgment. This research was supported by NIH and NSF and used instrumentation developed under NIH Grant RR 01348. The authors wish to thank Prof. David Wemmer for giving us the NMR coordinates of apamin. Valuable discussions with Ranjit Kumble and comments by S. Krimm are greatly acknowledged. Peter Hamm received the support of a postdoctoral fellowship granted by the Deutsche Forschungsgemeinschaft.

References and Notes

- (1) Krimm, S.; Bandekar, J. *J. Adv. Protein Chem.* **1986**, *38*, 181 and references therein.
- (2) Krimm, S.; Reisdorf, W. C., Jr. *Faraday Discuss.* **1994**, *99*, 181.
- (3) Reisdorf, W. C., Jr.; Krimm, S. *Biophys. J.* **1995**, *69*, 271.
- (4) Reisdorf, W. C., Jr.; Krimm, S. *Biochemistry* **1996**, *35*, 1383.
- (5) Mirkin, N. G.; Krimm, S. *J. Am. Chem. Soc.* **1991**, *113*, 9742.
- (6) Cheam, T. C.; Krimm, S. *J. Mol. Struct.* **1989**, *193*, 1.
- (7) Cheam, T. C.; Krimm, S. *THEOCHEM* **1989**, *57*, 15.
- (8) Torii, H.; Tasumi, M. *J. Chem. Phys.* **1992**, *96*, 3379.
- (9) Torii, H.; Tasumi, M. *Infrared Spectroscopy of Biomolecules*; Mantsch, H. H., Chapman, D., Eds.; Wiley-Liss: New York, 1996; pp 1.
- (10) Davydov, A. S. *Theory of Molecular Excitons*; Plenum: New York, 1971.
- (11) Baumruk, V.; Pancoska, P.; Keiderling, T. A. *J. Mol. Biol.* **1996**, *259*, 774.
- (12) Hill, J. R.; Tokmakoff, A.; Peterson, K. A.; Sauter, B.; Zimdars, D.; Dlott, D. D.; Fayer, M. D. *J. Phys. Chem.* **1994**, *98*, 11213.
- (13) Owrutsky, J. C.; Li, M.; Locke, B.; Hochstrasser, R. M. *J. Phys. Chem.* **1995**, *99*, 4842.
- (14) Pease, J. H. B.; Wemmer, D. E. *Biochemistry* **1988**, *27*, 8491.
- (15) Pagel, M. D.; Wemmer, D. E. *Proteins* **1994**, *18*, 205.
- (16) Martins, J. C.; van de Ven, F. J. M.; Borremans, F. A. M. *J. Mol. Biol.* **1995**, *253*, 590.
- (17) Deisenhofer, J.; Steigemann, W. *Acta Crystallogr. B* **1975**, *31*, 238.
- (18) Parkin, S.; Rupp, B.; Hope, H. *Acta Crystallogr. D* **1996**, *D52*, 18.

- (19) Janezic, D.; Venable, R. M.; Brooks, B. R. *J. Comput. Chem.* **1995**, *16*, 1554.
- (20) Janezic, D.; Brooks, B. R. *J. Comput. Chem.* **1995**, *16*, 1543.
- (21) Brooks, B.; Karplus, M. *Proc. Natl. Acad. Sci. U.S.A.* **1983**, *80*, 6571.
- (22) Roitberg, A.; Gerber, R. B.; Elber, R.; Ratner, M. A. *Science* **1995**, *268*, 1319.
- (23) Hamm, P.; Lim, M.; Hochstrasser, R. M. *J. Chem. Phys.* **1997**, *107*, 10523.
- (24) In the mid-IR spectral range, CaF₂ and BaF₂, used as beam splitters, polarizers, and windows in the IR cell, have a group velocity dispersion with signs opposite that of germanium, which was used for the long pass filter to block signal and idler. This fortunate situation permits minimization of the linear chirp by carefully selecting the path lengths of the different optical components.
- (25) Lian, T.; Kholodenko, Y.; Locke, B.; Hochstrasser, R. M. *J. Phys. Chem.* **1995**, *99*, 7272.
- (26) Yee, T. K.; Gustafson, T. K. *Phys. Rev A* **1978**, *18*, 1597.
- (27) Shen, Y. R. *The Principles of Nonlinear Optics*; Wiley: New York, 1984.
- (28) Mukamel, S. *Principles of Nonlinear Optical Spectroscopy*; Oxford: New York, 1995.
- (29) Joffre, M.; Hulin, D.; Migus, A.; Antonetti, A.; Guillaume, C. B.; Pegyhambarian, N.; Lindberg, M.; Koch, S. W. *Opt. Lett.* **1988**, *13*, 276.
- (30) Germer, T. A.; Stephenson, J. C.; Heilweil, E. J.; Cavanagh, R. R. *J. Chem. Phys.* **1993**, *98*, 9986.
- (31) Hamm, P. *Chem. Phys.* **1995**, *200*, 415.
- (32) Wynne, K.; Hochstrasser, R. M. *Chem. Phys.* **1995**, *193*, 211.
- (33) Both the perturbed free induction decay signal and the coherent two photon absorption signal have been observed to behave in same manner in experiments on small molecules (N₃⁻, CO₂), where the interpretation is clear since only one vibrational mode is involved. Hamm, P.; Lim, M.; Hochstrasser, R. M. To be published.
- (34) In the dynamic hole burning experiment, the ca. 1 ps pump pulse is asymmetric in time (see Materials and Methods), so delay zero is not well-defined. It was chosen 600 fs after the initial fast rise of the pump pulse.
- (35) One principal difference between refs 8 and 9 and our model should be mentioned: refs 8 and 9 follow the idea of a normal mode calculation, and consequently the coupling matrix contains forces while in our model the coupling Hamiltonian has the units of an energy.
- (36) The terminal carboxyl groups and carboxyl groups of amino acid side chains can be neglected since their frequency is somewhat lower or higher than the typical amide I frequency, depending on protonation, i.e., pH.
- (37) The fact that the location of the individual dipoles with respect to the peptide groups matters arises because the dipole approximation is used for V.
- (38) Model calculations were performed only for apamin (18 amino acids) and scyllatoxin (31 amino acids) but not for BPTI (58 amino acids) due to the large computer time which would have been needed. The dimension of the two-exciton matrix is $n(n+1)/2 \times n(n+1)/2$, and the computer time necessary to diagonalize this matrix increases with n .⁶ Diagonalizing of one sample matrix of one conformer of scyllatoxin takes ca. 1 min on a silicon graphics 2000 workstation and would take 45 h for BPTI.
- (39) Bernstein, F. C.; Koetzle, T. F.; Williams, G. J. B.; Meyer, E. F., Jr.; Brice, M. D.; Rodgers, J. R.; Kennard, O.; Shimanouchi, T.; Tasumi, M. *J. Mol. Biol.* **1977**, *112*, 535.
- (40) Abola, E. E.; Bernstein, F. C.; Bryant, S. H.; Koetzle, T. F.; Weng, J. In *Protein Data Bank, in Crystallographic Databases-Information Content*; Allen, F. H., Bergerhoff, G., Sievers, R. Eds.; Software Systems, Scientific Applications; Data Commission of the International Union of Crystallography: Bonn/Cambridge/Chester, 1987; pp 107–132.
- (41) Torii, H.; Tasumi, T.; Tasumi, M. *Mikrochim. Acta [Suppl.]* **1997**, *14*, 531.
- (42) Skinner, J. L. *J. Phys. Chem.* **1994**, *98*, 2503.
- (43) Meier, T.; Chernyak, V.; Mukamel, S. *J. Phys. Chem. B* **1997**, *101*, 7332.
- (44) Meier, T.; Zhao, Y.; Chernyak, V.; Mukamel, S. *J. Chem. Phys.* **1997**, *107*, 3876.
- (45) Thouless, D. *Phys. Rep.* **1974**, *13*, 93.
- (46) Schreiber, M.; Toyozawa, Y. *J. Phys. Soc. Jpn.* **1982**, *51*, 1537.
- (47) Davydov, A. S. *J. Theor. Biol.* **1977**, *66*, 379.
- (48) Davydov, A. S. *Phys. Scr.* **1997**, *20*, 387.
- (49) Freed, K. F.; Nitzan, A. *J. Chem. Phys.* **1980**, *73*, 4765.
- (50) Wynne, K.; Hochstrasser, R. M. *J. Raman Spectrosc.* **1995**, *26*, 561.
- (51) Owrutsky, J. C.; Raftery, D.; Hochstrasser, R. M. *Annu. Rev. Phys. Chem.* **1994**, *45*, 519.
- (52) Rey, R.; Hynes, J. T. *J. Chem. Phys.* **1998**, *108*, 142.
- (53) Laubereau, A.; Kaiser, W. *Rev. Mod. Phys.* **1978**, *50*, 607.
- (54) Oxtoby, D. W. *Adv. Chem. Phys.* **1981**, *47*, 487.
- (55) Seilmeier, A.; Kaiser, W. In *Ultrashort Laser Pulses*; Kaiser, W., Ed.; Springer: New York, 1993; p 279.
- (56) Fendt, A.; Fischer, S. F.; Kaiser, W. *Chem. Phys.* **1981**, *57*, 55.
- (57) Hochstrasser, R. M.; Anfinrud, P. A.; Diller, R.; Han, C.; Iannone, M.; Lian, T.; Lockke, B. In *Ultrafast Phenomena VII*; Harris, C. B., Ippen, E. P., Mourou, G. A., Zewail, A. H., Eds.; Springer Series in Chemical Physics, Vol. 53; Springer-Verlag: Berlin, Heidelberg, 1990; p 429.
- (58) Heilweil, E. J.; Casassa, M. P.; Cavanagh, R. R.; Stephenson, J. C. *Annu. Rev. Phys. Chem.* **1989**, *40*, 143.
- (59) Zinth, W.; Kolmeder, C.; Benna, B.; Irgens-Defregger, A.; Fischer, S. F.; Kaiser, W. *J. Chem. Phys.* **1983**, *78*, 3916.
- (60) Chen, X. G.; Schweitzer-Stenner, R.; Krimm, S.; Mirkin, N. G.; Asher, S. A. *J. Am. Chem. Soc.* **1994**, *116*, 11141.
- (61) Rey-Lafon, M.; Forel, M. L.; Garrigou-Lagrange, C. *Spectrochim. Acta A* **1973**, *29*, 471.
- (62) Mirkin, N. G.; Krimm, S. *J. Mol. Struct.* **1996**, *337*, 219.
- (63) Friedrich, J.; Haarer, D. *Angew. Chem., Int. Ed. Engl.* **1984**, *23*, 113.